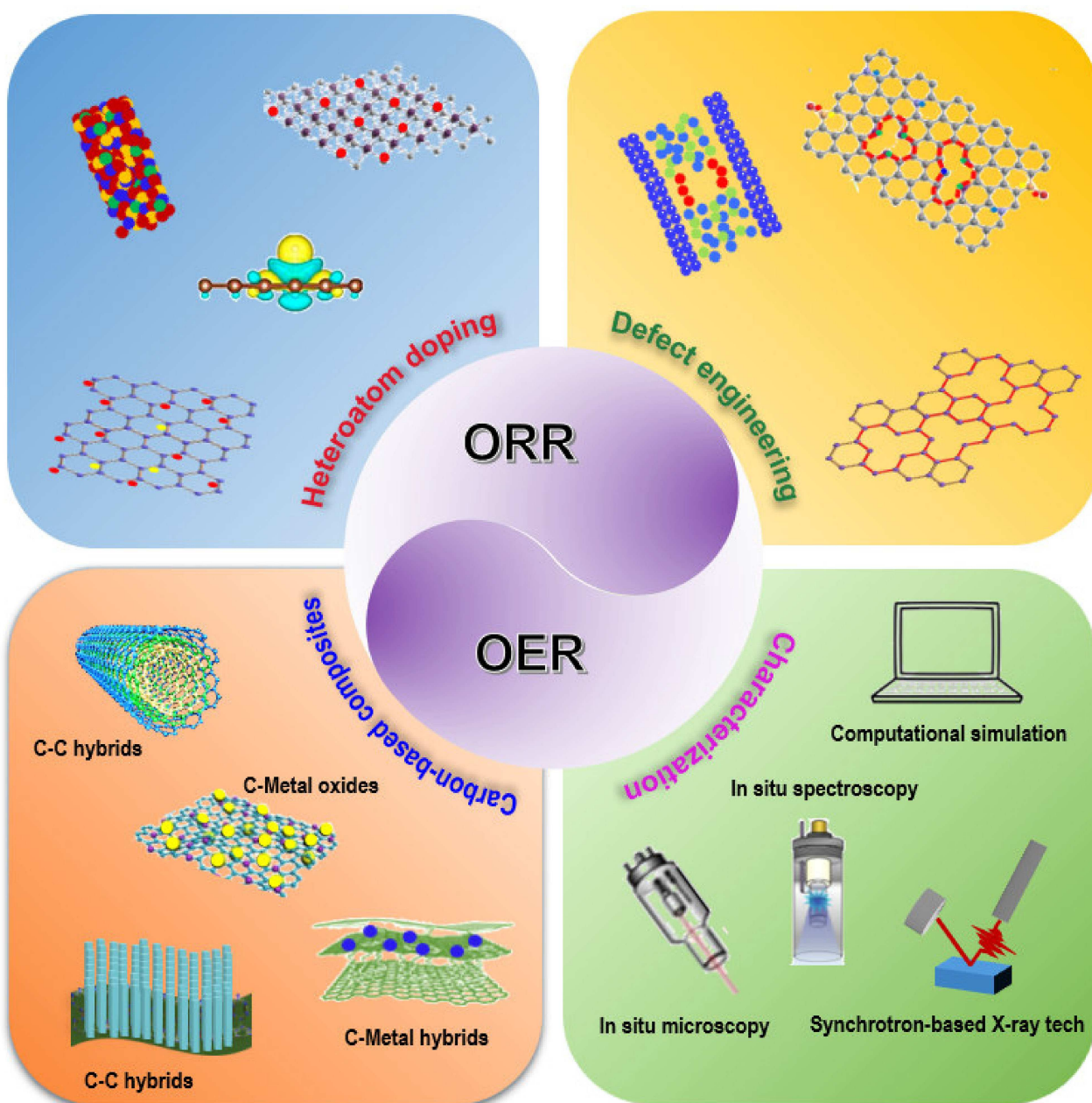


# Recent Advances in Carbon-Based Bifunctional Oxygen Catalysts for Zinc-Air Batteries

Daolan Liu<sup>+</sup><sup>[a]</sup>, Yueyu Tong<sup>+</sup><sup>[a]</sup>, Xiao Yan,<sup>\*[a, b]</sup> Ji Liang,<sup>\*[a]</sup> and Shi X. Dou<sup>[a]</sup>



Zinc-air batteries (ZABs) have recently received tremendous research attention due to their high theoretical energy densities. However, current ZABs suffer from poor energy efficiency and cyclability, mainly owing to the sluggish kinetics of the oxygen reduction reaction (ORR) and the oxygen evolution reaction (OER) on the air electrode. Therefore, rational design of efficient bifunctional oxygen electrocatalysts with high activity and stability is essential for improving battery performance. Carbon-based nanomaterials are promising candidates for bifunctional oxygen catalysis. In this review, we

present the latest development of carbon-based bifunctional electrocatalysts for ZABs. Firstly, the related reaction mechanisms of bifunctional ORR/OER catalysts are introduced. Then, the recent advances in developing carbon-based bifunctional catalysts with tailored structure and promising catalytic performance are introduced following the regulation strategies, e.g., heteroatom doping, defect engineering, and/or hybridizing with other active materials. Finally, the key challenges and perspectives of advanced ZABs are provided to better shed light on future research.

## 1. Introduction

With the ever-increasing demand for the transition from fossil fuels to clean and renewable energy, great efforts have been devoted to the development of sustainable energy harvesting, conversion, and storage. Batteries of various types have been an essential medium bridging energy harvesting and utilization. Li-ion batteries, due to the high energy storage capability, have successfully dominated the consumer market since their initial commercialization in the 1990s.<sup>[1–2]</sup> However, Li-ion batteries face a number of challenges, especially the safety issues and the uprising cost of battery materials.<sup>[1]</sup> To avoid these problems, the development of alternative electrochemical energy storage and conversion technologies (e.g., sodium-ion batteries,<sup>[3–4]</sup> lithium-metal batteries,<sup>[5]</sup> lithium<sup>[6–7]</sup> and non-lithium metal-sulfur batteries,<sup>[8–9]</sup> fuel cells,<sup>[10–11]</sup> and metal-air batteries<sup>[12–18]</sup>) has led to intensive research activity. Among them, metal-air batteries have gained special research interests due to their very high energy density, low cost, and environment-friendly operation. Metal-air batteries are assembled from a metal anode (e.g., Li, Na, K, Mg, Al, Zn) and an air-breathing cathode that are immersed in a proper electrolyte, generating electricity through the redox reaction between the metal anode and oxygen (Figure 1). The half-open structure of a metal-air battery allows the direct oxygen supply from ambient air as the cathode reactant, therefore enabling high capacities and energy densities. Among the available metal-air batteries, Zn-air batteries (ZABs) are considered a very promising battery system, because Zn is earth abundant and highly resistant against corrosion in alkaline solutions.<sup>[19–20]</sup> The high theoretical gravimetric energy density of ZABs ( $1086 \text{ W h kg}^{-1}$  including

oxygen<sup>[12]</sup> or  $1350 \text{ Wh kg}^{-1}$  excluding oxygen,<sup>[18]</sup> respectively) is much higher than that of the current lithium-ion technology. Moreover, ZABs can be potentially fabricated at a low cost of  $<10 \text{ $ kW}^{-1} \text{ h}^{-1}$ , two orders of magnitude lower than lithium-ion batteries ( $400\text{--}800 \text{ $ kW}^{-1} \text{ h}^{-1}$ ).<sup>[12,18]</sup> All these features make ZABs promising for future energy applications.

On the other hand, the major obstacles that limit the practical applications of ZABs are the overall energy efficiency and long-term cyclability, which are currently less than a quarter of the commercially available lithium-ion batteries.<sup>[21]</sup> The air electrode is the key factor that determines the battery performance, where the conversion between oxygen and metal hydroxide takes place. The intrinsic sluggish reaction kinetics on the air electrode, including oxygen reduction reaction (ORR) during the discharge process and oxygen evolution reaction (OER) during the charging process, contribute most to the high polarization and the inferior electrode reversibility of ZABs. Therefore, the rational design of efficient bifunctional oxygen catalysts has attracted intensive research interest with the purpose of accelerating the reaction kinetics and lowering the discharge/charge overpotentials to achieve better battery performances. So far, various materials have been explored as bifunctional oxygen electrocatalysts, including metal oxides, metal hydroxides, metal sulfides, carbon materials, and their composites.

Amongst, carbon materials are the most popular candidates to construct efficient bifunctional oxygen catalysts for ZABs, due to their high electrical conductivity, high chemical stability, versatile porous nanostructure, tunable physical and chemical properties, and low cost.<sup>[15,18,22–34]</sup> Remarkably, the electronic structure of carbon materials can be facilely modified via multiple regulation strategies (e.g., heteroatom doping,<sup>[26]</sup> defect engineering,<sup>[27]</sup> surface engineering,<sup>[29]</sup> etc.) to achieve variable electrocatalytic properties. In this review, we summarize the recent advances of carbon-based nanomaterials for efficient oxygen electrocatalysis and highlight their applications for rechargeable ZABs. Firstly, the related reaction mechanisms of bifunctional ORR/OER catalysts are introduced. Then, the emerging carbon-based bifunctional oxygen catalysts with tailored electronic nanostructure and promising catalytic performance are presented, categorized by the regulation strategies, including heteroatom doping, defect engineering, and/or hybridizing with other electrocatalytically active species (Figure 1). Finally, the existing challenges and future perspectives for the development of efficient oxygen catalysts for ZABs are

[a] D. Liu,<sup>+</sup> Y. Tong,<sup>+</sup> Dr. X. Yan, Dr. J. Liang, Prof. S. X. Dou  
Institute for Superconducting & Electronic Materials  
University of Wollongong  
North Wollongong, NSW 2500, Australia  
E-mail: liang@uow.edu.au

[b] Dr. X. Yan  
Guangdong Key Laboratory of Membrane Materials and Membrane Separation  
Guangzhou Institute of Advanced Technology, Chinese Academy of Sciences  
Guangzhou, 511458, China  
E-mail: xiao.yan@giat.ac.cn

[+] These authors contribute equally to this work.

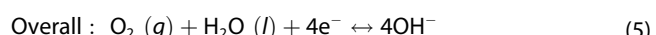
An invited contribution to a Special Collection dedicated to Metal-Air Batteries.



proposed. This review aims to provide timely information of the carbon-based bifunctional oxygen catalysts for researchers and to shed light on the future development of high-performance catalysts and ZABs.

## 2. Fundamentals of Oxygen Electrocatalysts

One critical issue for the current ZABs is their unsatisfying energy efficiency, less than 65% in most cases.<sup>[35]</sup> This is mainly due to the complex ORR/OER processes and their sluggish kinetics. Both ORR and OER involve a series of electrochemical processes that occur at the gas-liquid-solid interface, which usually involve mass diffusion, reactant/intermediate adsorption, charge transfer, bond cleavage, and product desorption. The reversible oxygen catalytic reactions on the air electrode consist of four elementary reaction steps in alkaline electrolyte:



(\* represents the active site)



Daolan Liu is currently pursuing her Ph.D. in the Institute for Superconducting and Electronic Materials at the University of Wollongong under the supervision of Dr. Ji Liang. Her research interests are focused on nanomaterials and electrocatalysts for energy conversion and storage.



Yueyu Tong is now a Ph.D. candidate in the Institute for Superconducting and Electronic Materials at the University of Wollongong under the supervision of Dr. Ji Liang and Prof. Shi Xue Dou. Her research interests are focused on advanced nanomaterials for renewable energy conversion and storage.



Xiao Yan is an Associate Professor at the Guangzhou Institute of Advanced Technology, Chinese Academy of Sciences. He received his Ph.D. from the Wolfson Centre for Materials Processing at Brunel University in 2012 and is currently a visiting researcher in the Institute for Superconducting and Electronic Materials of the University of Wollongong in Dr. Liang's group. His research interests are focused on porous nanomaterials and their

Generally, ORR starts with the diffusion of  $\text{O}_2$  to the solid catalyst surface and subsequent adsorption. The adsorbed oxygen molecule receives electrons to generate  $\text{HOO}^*$ ,  $\text{O}^*$ ,  $\text{HO}^*$ , and  $\text{OH}^-$  as intermediates and the final product through either a direct four-electron or a two-step two-electron transfer; while OER proceeds in the reverse direction. Compared with the two-step two-electron process, the direct four-electron route is more desirable for ZAB applications, due to its higher efficiency, which can be achieved with the rational design of electrocatalysts.

Both ORR and OER involve multiple oxygen-containing intermediates ( $\text{HOO}^*$ ,  $\text{O}^*$ ,  $\text{HO}^*$ ). The activity of the catalyst is strongly affected by the adsorption and dissociation of these intermediates. Theoretical calculations have revealed a universal scaling relationship between the adsorption energies of different intermediates on the catalysts' surface and their catalytic activities, including metals,<sup>[36–38]</sup> metal oxides,<sup>[39–40]</sup> and nanostructured carbons,<sup>[32,41]</sup> which can be used to predict the activity of the active sites.<sup>[42]</sup>

The Gibbs free energy change as a function of the adsorption energies in each elementary step in Equation (1)–(4) can be given by:

$$\Delta G_1 = \Delta G_{\text{OH}} \quad (6)$$

$$\Delta G_2 = \Delta G_{\text{O}} - \Delta G_{\text{OH}} \quad (7)$$

$$\Delta G_3 = \Delta G_{\text{OOH}} - \Delta G_{\text{O}} \quad (8)$$

applications in the energy and environmental fields.



Ji Liang received his Ph.D. from the University of Adelaide in 2014. After a two-year T. S. Ke Fellowship in the Institute of Metal Research of the Chinese Academy of Sciences, he was appointed an ARC-DECRA research fellow in the Institute for Superconducting and Electronic Materials of the University of Wollongong, Australia. His research interests lie in the design of functional carbon-based materials for electrochemical catalysis and energy storage applications.



Prof. Shi Xue Dou is the director of Institute for Superconducting and Electronic Materials and a Distinguished Professor at the University of Wollongong. He received his Ph.D. in chemistry in 1984 at Dalhousie University, Canada and his D.Sc. at the University of New South Wales in 1998. He was elected as a Fellow of the Australian Academy of Technological Science and Engineering in 1994. He is a program leader for the Automotive Corporate Research Center-2020.

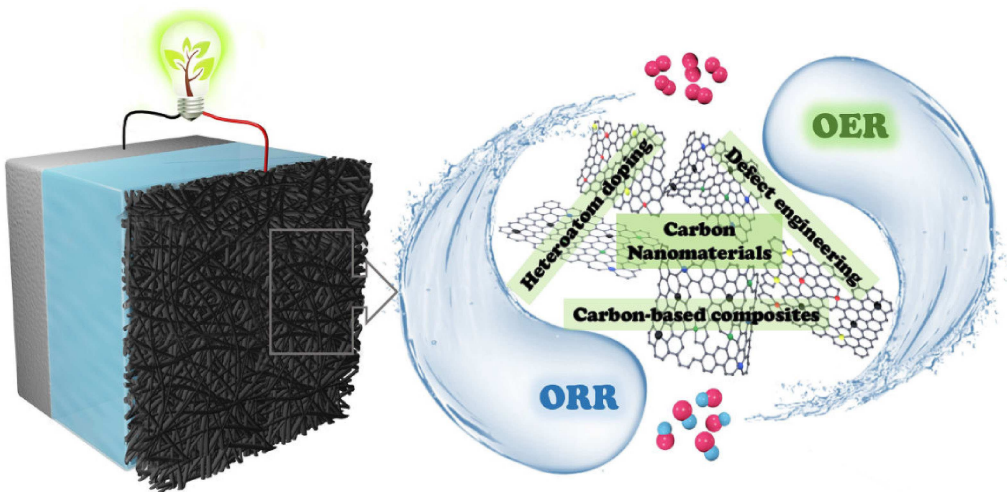


**Figure 1.** Metal-air battery and carbon nanomaterials as bifunctional oxygen catalysts.

$$\Delta G_4 = \Delta G_{O_2} - \Delta G_{OOH} \quad (9)$$

Due to this scaling relationship, the adsorption energies of the intermediates on the active sites are correlated and therefore can be expressed by the adsorption energy of one of them. Nørskov et al. presented the theoretical volcano plots of the ORR and OER activity on metal oxide (Figure 2a) and metal (Figure 2b) surfaces by calculating the Gibbs free energies in each elementary step as a function of the binding energy of the oxygen-containing intermediates.<sup>[37]</sup> As can be seen, the ORR activity is restricted by the OH\* reduction step (black line) and O<sub>2</sub> reduction steps (blue line), and the OER activity is limited by the HOO\* (green line) and O\* formation step (red line). The adsorption energies of the oxygen-containing intermediates for the most active ORR and OER sites are not identical, meaning that a catalyst cannot simultaneously achieve the best ORR and OER activities. Through proper regulation on the surface geometry and electronic structure of the catalyst, however, the vertices of ORR and OER volcanos can be bridged to certain extent to achieve a satisfactory bifunctional catalytic activity.

In practice, several parameters are commonly used as the descriptors to evaluate the performance of bifunctional oxygen electrocatalysts. These parameters include the potential to achieve the current density of  $10 \text{ mA cm}^{-2}$  ( $E_{10}$ ) for OER catalysis, the potential to reach half of the limiting current density (half-wave potential,  $E_{1/2}$ ) for ORR catalysis, and the potential gap ( $\Delta E$ ) between  $E_{10}$  and  $E_{1/2}$  for bifunctional oxygen catalysis. Sometimes, the bifunctional catalytic activity is also evaluated by the potential gap between the  $E_{10}$  and the ORR current density at  $-3 \text{ mA cm}^{-2}$  ( $E_{-3}$ ), which approximates the theoretical half-wave potential value of the four-electron ORR pathway measured on a typical rotating-disc electrode.<sup>[43]</sup> Generally, the smaller the potential gap is, the better the bifunctional performance the catalyst can deliver.<sup>[18]</sup>

### 3. Carbon-Based Bifunctional Oxygen Catalysts

Carbon-based materials, such as carbon nanotubes (CNTs), graphene/graphene oxide (GO)/reduced graphene oxide (rGO), graphitic carbon nitride (g-C<sub>3</sub>N<sub>4</sub>), and their hybrids have been proven capable of facilitating the electron transfer and mass diffusion for ORR/OER. Moreover, their electronic structures can be readily regulated with heteroatom-doping, rational defect engineering, or coupled with other species, leading to improved catalytic performance.

#### 3.1. Heteroatom-Doped Nanocarbons

Deliberately introduced heteroatoms, such as N, B, O, S, P, can effectively tune the local electronic structure and the charge density distribution of adjacent carbon atoms, leading to enhanced electrocatalytic activity of the carbon nanomaterials.<sup>[29]</sup>

N-doped carbons are among the most widely investigated nanomaterials during the exploration for efficient bifunctional

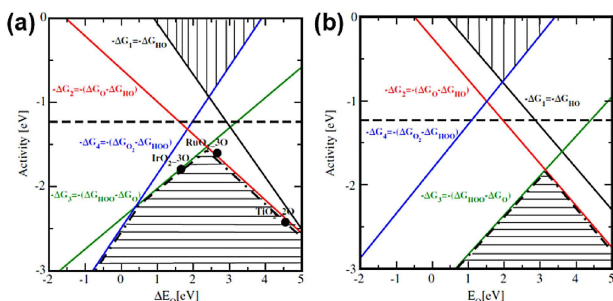


**Figure 2.** Theoretical ORR and OER activity volcano plots on a) metal oxide and b) metal surfaces as a function of oxygen binding energy. Reproduced with permission.<sup>[37]</sup> Copyright 2007, Elsevier

oxygen catalysts.<sup>[44–47]</sup> The active sites of N-doped nanostructured carbon for oxygen catalysis are attributed to both electron-donating quaternary N sites (n-type doping) are responsible for enhanced ORR activity by providing electrons to the  $\pi$ -conjugation of the carbon rings, leading to increased nucleophile strength and enhanced  $O_2$  adsorption; whereas the electron-withdrawing pyridinic N moieties (p-type doping) facilitate the adsorption of water oxidation intermediates, resulting in improved OER activity (Figure 3a).<sup>[48]</sup>

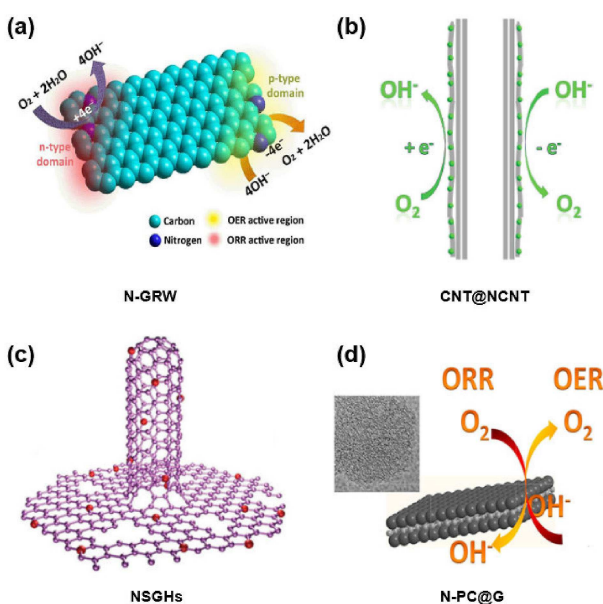


**Figure 3.** N-doped nanocarbons for bifunctional oxygen catalysis. a) N-doped graphene nanoribbons. Reproduced with permission.<sup>[48]</sup> Copyright 2016, American Association for the Advancement of Science. b) CNT@NCNT coaxial nanocables with surface enriched nitrogen. Reproduced with permission.<sup>[44]</sup> Copyright 2014, Wiley-VCH. c) N-doped graphene/carbon nanotube hybrids. Reproduced with permission.<sup>[45]</sup> Copyright 2014, Wiley-VCH. d) Sandwich-like structured N-doped porous carbon@graphene. Reproduced with permission.<sup>[49]</sup> Copyright 2016, Elsevier.

Pioneering work was reported in 2014 on the investigation of the N-doped and coaxial carbon nanocables (CNT@NCNT)<sup>[44]</sup> and N-doped graphene/single-walled CNT (SWCNT) hybrids (NSGHs).<sup>[45]</sup> Both catalysts exhibited promising bifunctional activity because of their structural advantages. The CNT@NCNT coaxial nanocables have abundant surface N atoms serving as the active sites and well-preserved inner CNT wall facilitating fast electron transfer (Figure 3b); while the NSGHs contain N-containing functional groups evenly distributed in a highly conductive scaffold of simultaneously grown graphene/SWCNT (Figure 3c). Moreover, the NSGHs possess a large specific surface area of  $812.9\text{ m}^2\text{ g}^{-1}$ . All these structural features contribute to potential gaps of 0.95 and 1.05 V in 0.1 M KOH electrolyte, respectively, indicating good bifunctional catalytic performance.

Besides, a sandwich-like structured N-doped porous carbon@graphene (N-PC@G) composite has also been reported with superior bifunctional catalytic activity towards ORR/OER ( $\Delta E=0.83\text{ V}$ ).<sup>[49]</sup> This arises from the unique structure features,

including the large surface area and hierarchically porous structure that are favourable for the exposure of active sites and the high graphitization degree that is beneficial for the fast electron transfer (Figure 3d).

Besides nitrogen, other heteroatoms (e.g., B, P, O, S) have also been doped into carbon matrix to modify the electron and charge distribution around the heteroatom dopants, leading to improved electroactivity.<sup>[47,50–53]</sup> For instance, stable C–S–C active sites (Figure 4a) have been generated on S-doped CNTs

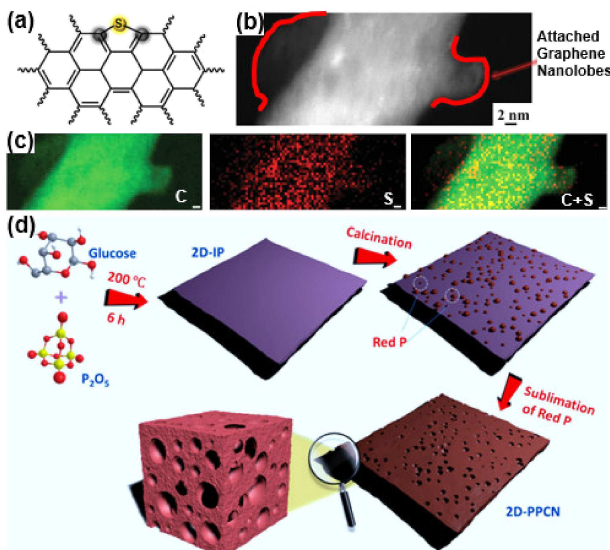


**Figure 4.** a) Schematic illustration of sulfur-doped carbon nanotubes. b–c) High-angle annular dark field scanning transmission electron microscopy (HAADF-STEM) image of bi-doped carbon nanotube (S, S'-CNT<sub>1000 °C</sub>) and the corresponding elemental mapping (scale bar: 2 nm). Reproduced with permission.<sup>[50]</sup> Copyright 2016, Wiley-VCH. d) Schematic illustration of the synthesis route for 2D-PPCN. Reproduced with permission.<sup>[53]</sup> Copyright 2018, American Chemical Society.

through a bi-doping strategy.<sup>[50]</sup> Partially unzipped CNTs were firstly hydrothermally treated at 180 °C with thiourea to form S-CNT180 °C, which were then pyrolyzed at 1000 °C in the presence of benzyl disulfide (BDS) to produce bi-doped S, S'-CNT<sub>1000 °C</sub>. The S, S'-CNT<sub>1000 °C</sub> shows outstanding bifunctional catalytic performance ( $E_{10}=1.58\text{ V}$  and  $E_{1/2}=0.79\text{ V}$ ), due to that BDS can generate stable active sites and CNT defects by forming graphene nanolobes attached to the CNT walls (Figure 4b–c).

Another two-dimensional P-doped carbon nanosheets (2D-PPCN) with tunable porosity were also reported to catalyse the oxygen reactions in ZABs (Figure 4d).<sup>[53]</sup> The P dopants induce structural defects and electron delocalization due to their electron donating capability, endowing the 2D-PPCN with enriched active sites and improved conductivity for electron transfer. Moreover, the 2D-PPCN also possesses a hierarchically porous structure to expose abundant active sites on its surface and to facilitate the mass transport during the catalytic process. Therefore, this 2D-PPCN material showed well-balanced ORR ( $E_{1/2}=0.85\text{ V}$ ) and OER ( $E_{10}=1.60\text{ V}$ ) catalytic activity.

Compared with the mono-element doping strategy, doping carbons with multiple heteroatoms has been proven effective for enhancing the electrocatalytic activity by modulating the electronic properties and surface polarities of nanostructured carbon materials.<sup>[24,26,29,54–55]</sup> For example, an N, P co-doped porous carbon foam (NPMC) was fabricated as an efficient bifunctional O<sub>2</sub> electrocatalyst for ZABs.<sup>[56]</sup> This NPMC with a three-dimensional (3D) structure was obtained by pyrolyzing the polyaniline (PANI) aerogels that were synthesized with phytic acid (PA) as the crosslinker and protonic dopant (Figure 5a). The NPMC possesses a hierarchical porous network

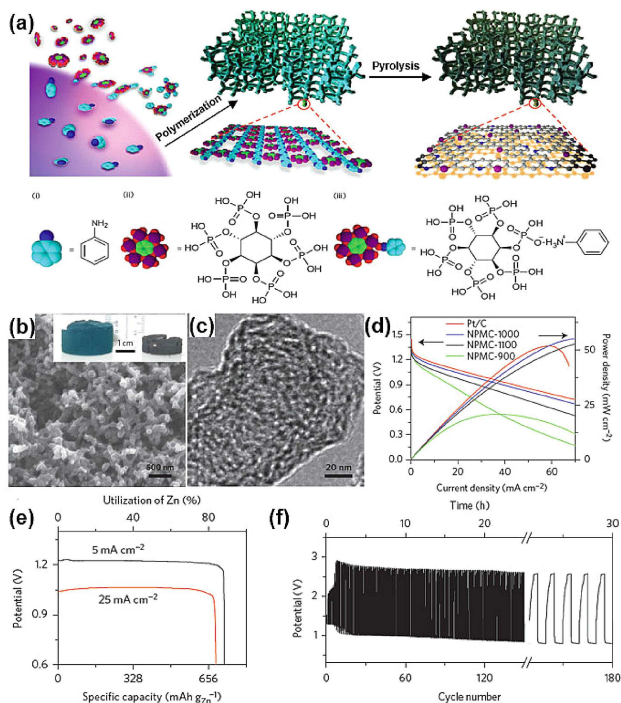


**Figure 5.** a) Schematic illustration of the preparation process for the NPMC foams. b) Scanning electron microscopy (SEM) image of NPMC-1000. The inset shows the digital photo images of PANI aerogel before (left) and after (right) pyrolysis at 1000 °C. c) High-resolution transmission electron microscopy (HR-TEM) image of NPMC-1000. d) The linear scan voltammogram (LSV) curves of different catalysts for both ORR and OER in 0.1 M KOH at 1600 rpm (scan rate: 5 mV s<sup>-1</sup>). e) Schematic of the basic configuration of a primary ZAB. f) Discharge/charge cycling curves of two-electrode rechargeable ZABs at a current density of 2 mA cm<sup>-2</sup> using the NPMC-1000 air electrode. Reproduced with permission.<sup>[56]</sup> Copyright 2015, Springer Nature.

with abundant N, P-coupled graphene edge sites in the individual mesoporous ligaments (Figure 5b, c). DFT calculations suggested that the N, P co-doping can generate synergistic effects, resulting in the minimum overpotentials for ORR (0.44 V) and OER (0.39 V). The NPMC shows an outstanding bifunctional activity, with an ORR  $E_{1/2}$  of 0.85 V and an even lower OER onset potential than RuO<sub>2</sub> catalyst. The air electrodes with this NPMC electrocatalyst were further used in both primary and rechargeable ZABs. The primary ZABs exhibited an open circuit potential of ~1.48 V, an energy density of ~835 Wh kg<sup>-1</sup>, a peak power density of 55 mW cm<sup>-2</sup>, and a stable operation for 240 h after mechanical recharging (Figure 5d, e).

On the other hand, the rechargeable ZABs also showed good stability (180 cycles at 2 mA cm<sup>-2</sup>, Figure 5f).

Excellent bifunctional activity was also achieved on N and P co-doped graphene/carbon nanosheets (N, P-GCNS), obtained by the pyrolysis of a dry hydrogel composed of graphene oxide, PANi, and PA (Figure 6a).<sup>[57]</sup> The sandwich-like hierarchi-

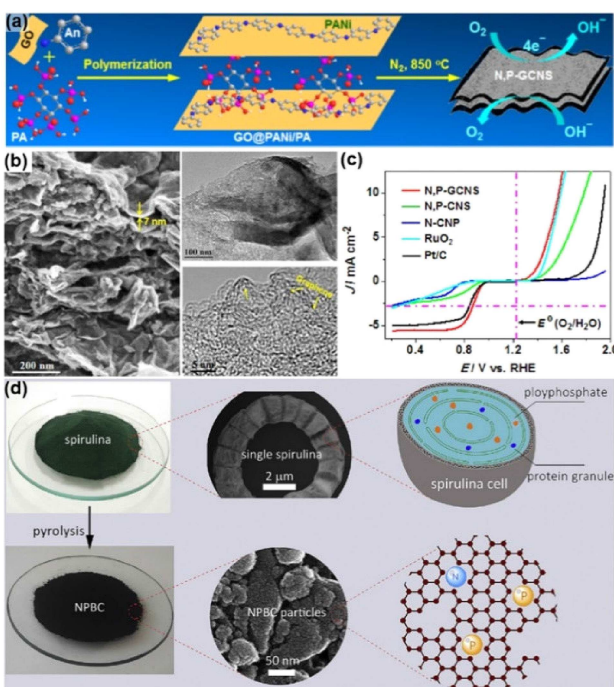


**Figure 6.** a) Schematic illustration of the fabrication process and structure of N, P-GCNS. b) SEM (left) and TEM (right) images of N, P-GCNS. c) Bifunctional catalytic activity of various catalysts toward both ORR and OER. Reproduced with permission.<sup>[57]</sup> Copyright 2015, American Chemical Society. d) Schematic illustration of the single-step synthesis of NPBC from the nitrogen and phosphorus-rich microalgae. Reproduced with permission.<sup>[61]</sup> Copyright 2017, Elsevier.

cally porous structure of this material, with ultrafine N, P-doped carbon particles attached on both sides of wrinkled graphene nanosheets (Figure 6b), endowed the N, P-GCNS with highly exposed active sites and fast electron transportation. Thus, enhanced bifunctional electrocatalytic activity with  $\Delta E = 0.72$  V has been achieved on this material (Figure 6c). Besides, other carbon nanostructures co-doped with N and P atoms have been extensively investigated as well, including nanospheres,<sup>[58]</sup> microtubes,<sup>[59]</sup> and 3D hierarchical porous graphene.<sup>[60]</sup> Recently, a very simple and cost-effective pyrolysis method has been reported for the mass production of N, P co-doped mesoporous biocarbon (NPBC) for ZABs.<sup>[61]</sup> The NPBC was obtained by high-temperature pyrolysis of spirulina, an industrially cultivated microalgae that is rich in proteins and phosphates (Figure 6d). The NPBC exhibited an  $E_{1/2}$  of 0.86 V, an  $E_{10}$  of 1.68 V, and a narrow potential gap of only 0.82 V, indicating its superb ORR/OER bifunctional electrocatalytic activity. The primary and rechargeable ZABs using NPBC as air electrodes delivered a high discharge power density of 90.7 mW cm<sup>-2</sup> and a high energy density of 850 Wh kg<sup>-1</sup> in

ambient condition. Graphitic carbon nitride ( $\text{g-C}_3\text{N}_4$ ) with ultra-high N content (theoretically up to 60 wt.%) has been utilized for efficient ORR and OER bifunctional catalysis as well because the high N content can provide abundant active sites.<sup>[62–63]</sup> Ma et al. reported a bifunctional and P-doped  $\text{g-C}_3\text{N}_4$  (P-g-C<sub>3</sub>N<sub>4</sub>) nanoflower that was *in situ* grown on carbon-fiber paper (PNP/CFP).<sup>[64]</sup> This PNP/CFP exhibits high activity ( $\Delta E = 0.96$  V) and high stability in reversible ORR and OER, thanks to the combined merits from homogeneous distribution of the N, P dopants, strong coupling between P-g-C<sub>3</sub>N<sub>4</sub> and CFP facilitating electron transfer, and the 3D nanostructure that guarantees enhanced mass transfer and high active surface area.

It is worth noting that although superior bifunctional activity has been achieved on the N, P co-doped carbon materials, the actual active sites for ORR and OER are still unclear. Guo et al. investigated the bifunctional P and N co-doped graphene framework (PNGF) using combined computational calculations and rational selection of P/N precursors.<sup>[65]</sup> The P–N bonds are identified to be favourable for OER, and the local structures with sole N dopants are responsible for the ORR activity, respectively. In contrast, Liu et al.<sup>[66]</sup> recently studied another nanostructured carbon consisting a single-walled carbon nanotube conductive network embedded in porous N, P co-doped carbon (SWCNT@NPC), and claimed that the N, P co-doping sites are active for ORR, and the N doping sites are the primary active sites for OER. The controversial outcome indicates that more efforts should be devoted to the identification of the specific active sites in the bifunctional oxygen catalysts.

Other types of heteroatoms have also been exploited to dope carbon materials, such as N and S,<sup>[51,67–69]</sup> N and B,<sup>[70]</sup> P and S,<sup>[71–72]</sup> N and O,<sup>[73–74]</sup> et al. Dai and co-workers prepared N and O co-doped nanoporous carbon nanofiber films (NCNFs) by high-temperature pyrolysis of electrospun polyimide (PI) fiber films as bifunctional catalysts (Figure 7a–c).<sup>[75]</sup> At high pyrolysis temperatures (550–800 °C), the nitrogen species in the aromatic structure of PI decomposed into N-containing gaseous compounds (e.g., HCN and NH<sub>3</sub>), which served as the source for N-doping and activation of the resulted NCNFs.<sup>[75]</sup> Moreover, the NCNFs also contain ketonic oxygen-containing groups (e.g., C=O and C–O), which can alter the electronic structures of the adjacent carbon atoms and facilitate the adsorption of OER intermediates.<sup>[76]</sup> Consequently, the NCNFs showed an excellent ORR ( $E_{1/2} = 0.82$  V) and OER ( $E_{10} = 1.84$  V) bifunctional activity (Figure 7d), due to the uniform distribution of active sites containing N and O dopants, large specific surface area, and high electrical conductivity. The rechargeable ZABs based on this NCNF air cathodes exhibited a small charge-discharge voltage gap (~0.73 V @ 10 mA cm<sup>-2</sup>), high reversibility (initial round-trip efficiency of 62%), and high stability (voltage gap increasing by merely ~0.13 V after 500 cycles, Figure 7e–g).

Another common strategy is the N and S co-doping. For example, Chen and co-workers reported an N, S dual-doped and activated commercial carbon cloth (N, S-CC), which was prepared through a multi-step and *in situ* activating strategy, as an “all in one” air electrode for flexible and rechargeable ZABs (Figure 8a).<sup>[67]</sup> Through *in situ* texturing and surface

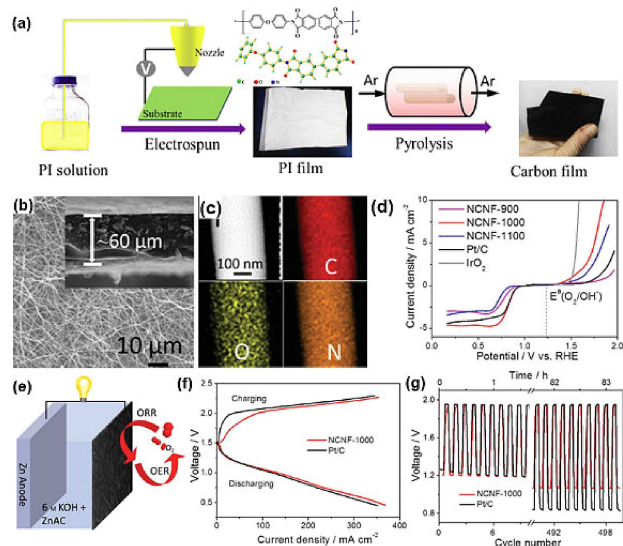


**Figure 7.** a) Schematic representation of the fabrication procedure to the NCNF. b) SEM image of NCNF-1000 with the inset showing the thickness. c) STEM images and corresponding elemental mapping images of C, O, N of NCNF-1000. d) LSV curves of different catalysts for both ORR and OER in 0.1 M KOH at 1600 rpm (scan rate: 5 mV s<sup>-1</sup>). e) Schematic representation of the rechargeable ZAB. f) Charge and discharge polarization curves. g) Galvanostatic discharge-charge cycling curves at 10 mA cm<sup>-2</sup> of rechargeable ZABs with the NCNF-1000 and Pt/C as the catalyst, respectively. Reproduced with permission.<sup>[73]</sup> Copyright 2016, Wiley-VCH.

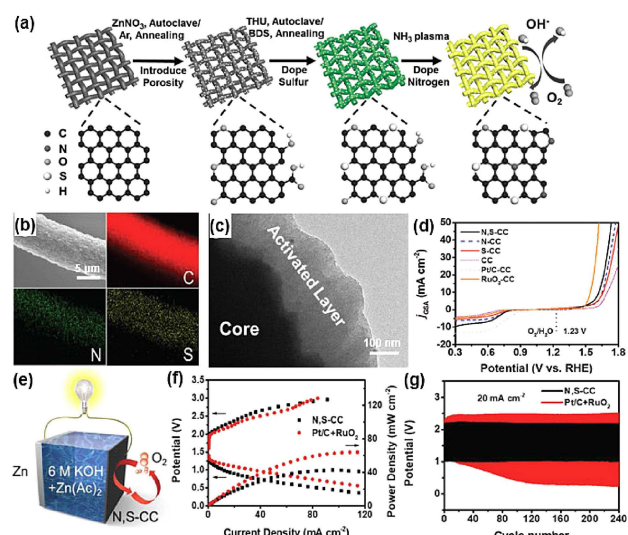


**Figure 8.** a) Schematic illustration for the preparation of N, S-CC. b) SEM image of individual N, S-CC fiber and the corresponding elemental mapping images. c) TEM image of individual N, S-CC fiber. d) Overall polarization curves of different catalysts within the ORR and OER potential window in 1 M KOH. e) Schematic representation of liquid rechargeable ZABs. f) Polarization and power density curves of batteries. g) Galvanostatic discharge-charge cycling curves at 20 mA cm<sup>-2</sup>. The charge/discharge depth: 600 s cycle<sup>-1</sup>. Reproduced with permission.<sup>[67]</sup> Copyright 2018, Wiley-VCH.

engineering, the N, S-CC possessed a large surface area and hierarchical meso-micro porosity for improved mass transport and enlarged active surface area. Moreover, this N, S-CC also had a unique core-shell structures with a uniform distribution N, S dopants on the activated carbon shell (Figure 8b, c) to

expose a large number of active sites for ORR/OER, resulting in superior catalytic performance with a very small  $\Delta E$  of 0.87 V (Figure 8d). The rechargeable ZAB equipped with this free-standing N, S-CC air electrode delivered a comparably small charge-discharge voltage gap with the Pt/C + RuO<sub>2</sub> catalyst and a high peak power density of 42 mW cm<sup>-2</sup> (Figure 8e, f). Remarkably, this ZAB also possessed stable charge/discharge voltages with negligible voltage fading when cycled at various current densities (0.5–5 mA cm<sup>-2</sup>) or even at a much higher current density of 20 mA cm<sup>-2</sup> (Figure 8g).

Other nanostructured carbons with N, S dual dopants, like N, S co-doped carbon nanosheets,<sup>[51]</sup> 2D graphitic sheets consisting of stereoscopic holes over the graphitic surface,<sup>[68]</sup> 3D hierarchical carbon nanocages,<sup>[69]</sup> and hierarchically porous carbon,<sup>[77]</sup> have also been synthesized with excellent bifunctional electrochemical performances, due to their synergistic effect from the N, S interaction and unique structural features.

Moreover, ternary-doped carbon materials have also been investigated as bifunctional oxygen catalysts.<sup>[78–80]</sup> As mentioned above, g-C<sub>3</sub>N<sub>4</sub> has multiple merits for oxygen electrocatalysis, including high N content, stable molecular structure, and tailorable electronic structure.<sup>[81]</sup> Heteroatom doping of g-C<sub>3</sub>N<sub>4</sub> has the potential of further boosting the catalytic activity by altering its surface polarity and electronic properties.<sup>[41]</sup> Lee et al. produced P and S co-doped g-C<sub>3</sub>N<sub>4</sub> sponges (P, S-CNS) by polymerization and pyrolysis of aminoguanidine (Figure 9a).<sup>[71]</sup>

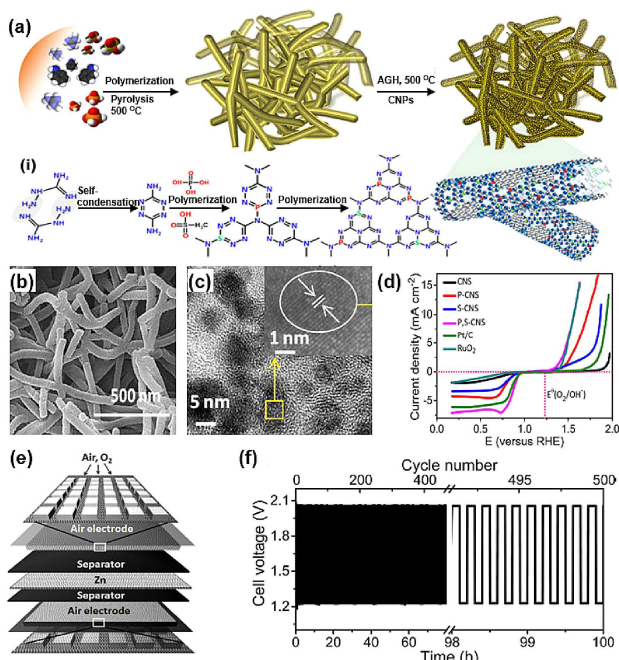


**Figure 9.** a) Schematics showing the synthesis of P, S-CNS catalysts, and (i) the reaction mechanism for the formation of the C–N polymeric complex. b) SEM image of the sponge-like P, S-CNS with randomly entangled nanotubes. c) HR-TEM image of the embedded carbon nanoparticles (CNPs) with the inset showing the (100) spacing of graphitic carbon. d) LSV plots of the ORR and OER for different catalysts at 1600 rpm in 0.1 M KOH (scan rate: 5 mV s<sup>-1</sup>). e) Schematic illustration of a trielectrode ZABs. f) Trielectrode rechargeable ZABs galvanostatic charge/discharge cycles with P, S-CNS as the bifunctional catalyst. Reproduced with permission.<sup>[71]</sup> Copyright 2017, American Chemical Society.

The P, S-CNS exhibits a 3D hierarchical network structure of randomly entangled carbon nitride nanotubes (ca. 60 nm) embedded with carbon nanoparticles (5–30 nm in diameter, Figure 9b, c), contributing to a large active surface area and plentiful edge-sites for promising catalytic activity. As a result, the P, S-CNT delivered superior bifunctional catalytic performance compared to Pt/C and RuO<sub>2</sub>, respectively, with a low half-wave potential (ca. 0.87 V), superior limiting current density (7.14 mA cm<sup>-2</sup>) for ORR and very low overpotential (0.33 V) for OER (Figure 9d). A rechargeable ZAB with a three-electrode configuration was assembled by utilizing this P, S-CNS material as the decoupled ORR and OER electrodes with a sandwiched Zn electrode (Figure 9e), which showed a smaller charge-discharge voltage polarization of ca. 0.80 V at a current density of 25 mA cm<sup>-2</sup>, signifying its good rechargeability. Furthermore, the ZAB showed better stability over 500 cycles with continuous operation for 100 h (Figure 9f).

The same group also reported *in situ* grown and P, S co-doped carbon nitride fibers (PS-CNFs) on carbon cloth as flexible oxygen electrodes for ZABs.<sup>[72]</sup> The PS-CNTs showed an ultra-high surface area (1649 m<sup>2</sup> g<sup>-1</sup>) and good electrical conductivity (165 Sm<sup>-1</sup>), leading to excellent battery performances for both primary and rechargeable ZABs. Recently, N, F, P ternary dopants were introduced into macro-porous carbon fibers (NFPC), which was prepared by electrospinning the mixture solution of NaPF<sub>6</sub> and polyacrylonitrile dissolved in *N*, *N*-dimethylformamide and subsequent thermal treatment.<sup>[82]</sup> The NFPC possessed a large specific surface area, which can provide more exposed active sites and facilitate the mass transfer, along with the synergistic effect of heteroatoms, leading to enhanced ORR and OER bifunctional activity. The primary ZAB with this NFPC electrode catalyst delivered a discharge capacity of 520 mAh g<sup>-1</sup> at 10 mA cm<sup>-2</sup>, and the rechargeable ZAB showed excellent cycling stability with no obvious potential decay after 200 charge-discharge cycles, outperforming those catalysed by Pt/C + RuO<sub>2</sub>.

### 3.2. Defect-Rich Nanocarbons

Defects in the carbon framework, such as intrinsic structural and edge defects (e.g., pentagonal, zigzag edge, Stone-Wales defects) or defects induced by heteroatom doping, are practically inevitable. Recently, both theoretical and experimental investigations have revealed that such defects can alter the charge or spin distribution of the sp<sup>2</sup> carbon plane, leading to enhanced intermediate chemisorption and accelerated electron transfer, which are favourable for electrocatalysis processes.<sup>[26–27,30]</sup> Yao et al. created various carbon defects (pentagons, heptagons, and octagons) via a facile nitrogen removal procedure from the N-doped graphene (NG), as illustrated in Figure 10a.<sup>[83]</sup> Density functional theory (DFT) calculations showed that the edge atoms around the three special defects (pentagon, pentagon-octagon-pentagon, and heptagon-pentagon-pentagon-heptagon, Figure 10b) contribute to the highest occupied molecular orbital and lowest unoccupied molecular orbital, yielding catalytic activities for

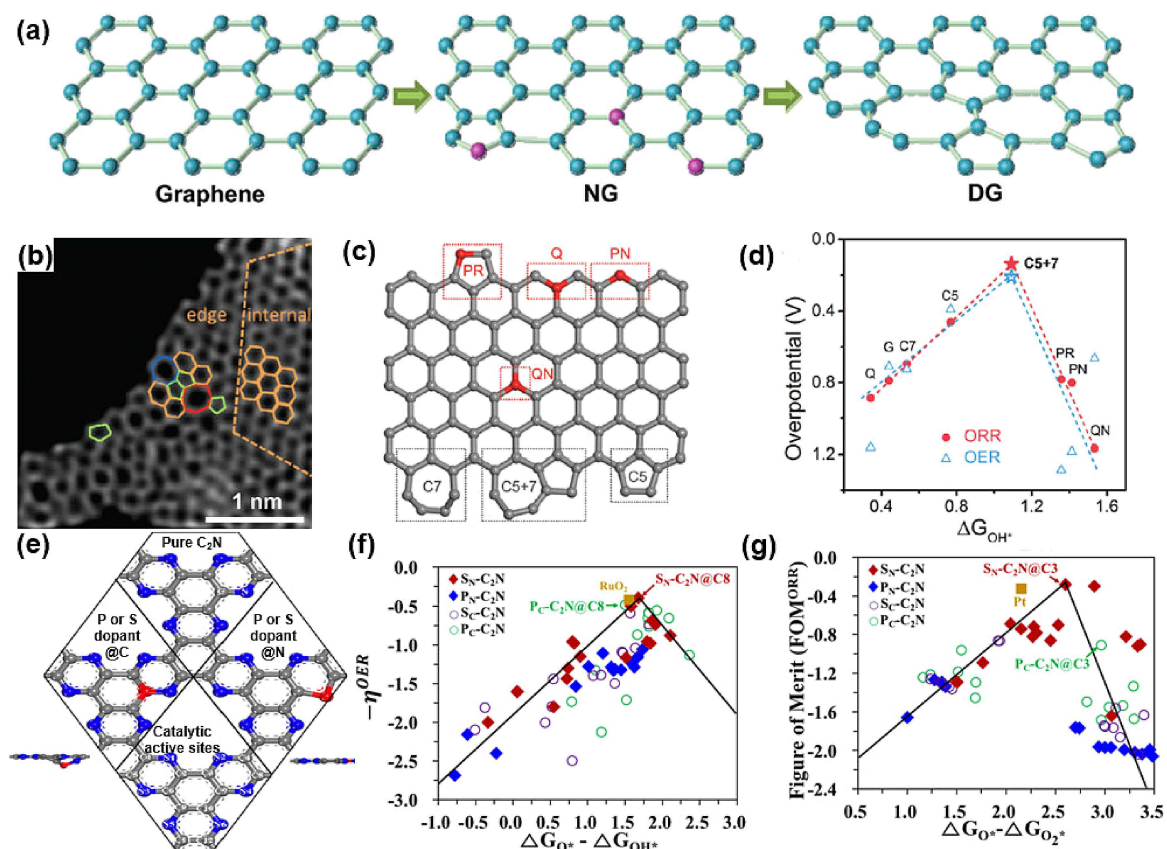


**Figure 10.** a) Schematic of the formation of carbon defects in 2D graphene (DG). b) HAADF-STEM image of DG showing various carbon defects. Reproduced with permission.<sup>[83]</sup> Copyright 2016, Wiley-VCH. c) Schematic graphene nanoribbon with various defects. d) ORR and OER volcano plots of overpotential versus adsorption free energy of  $\text{OH}^*$ . Reproduced with permission.<sup>[84]</sup> Copyright 2016, Wiley-VCH. e) Schematic of the heteroatom-doped nitrogenated holey structure ( $X_yC_2N$ ). f, g) OER and ORR volcano plots for  $P_c\text{-C}_2\text{N}$  and  $P_n\text{-C}_2\text{N}$ ,  $S_c\text{-C}_2\text{N}$  and  $S_n\text{-C}_2\text{N}$  catalysts. Reproduced with permission.<sup>[85]</sup> Copyright 2018, American Chemical Society.

both ORR and OER. Zhang and co-workers systematically studied all the possible active sites (e.g., N-doping sites, topological defects, and edge defects, Figure 10c) using DFT computations.<sup>[84]</sup> The ORR and OER volcano plots of the overpotential for each active sites were plotted as a function of the adsorption energy of  $\text{OH}^*$ , indicating the dopant-free topological defects composed of adjacent pentagon and heptagon (C5 + 7) are the optimal active sites for both ORR and OER (Figure 10d). As a result, the N-doped and defect-rich graphene mesh (NGM) delivered the excellent ORR/OER bifunctional activities ( $\Delta E = 0.90$  V in 0.1 M KOH) and ZAB performance. Hierarchically designed 3D holey aerogels modulated with S or P dopants have also been reported as bifunctional  $\text{O}_2$  electrodes for flexible and rechargeable ZABs.<sup>[85]</sup> The large S or P dopant can generate out of plane structural deformations (at C sites) and structural strain with elongated C–S or C–P bond (at N sites), resulting in unsaturated  $\text{sp}^3\text{-C}$  and  $\text{sp}^3\text{-N}$  geometries. The activity of vicinal sites of dopant can, therefore, be increased for favorable sorption of reaction intermediates at the N- and defect-rich sites. DFT calculations reveal that S dopants on N sites ( $S_n\text{-C}_2\text{N}$ ) show the best ORR/OER performance (Figure 10e–g).

In general, heteroatom doping often induces crystalline disorder and representative defects, such as vacancies, lattice

reconstruction, and dangling groups, which could also significantly enhance the catalytic activities.<sup>[87]</sup> Extensive research efforts have been devoted to investigating the nanostructured carbon with both heteroatom doping and abundant structural defects for oxygen catalysis in ZABs.<sup>[27,85–86,88–92]</sup> Studt et al. reported an  $\text{NH}_3$ -activated and N-doped hierarchical carbon (NHC) as a high-performance and low-cost ORR/OER bifunctional catalyst.<sup>[86]</sup> The NHC consisted of both structural defects and heteroatom dopants as the active sites (Figure 11a, b). All the possible active sites (Figure 11c), contributing to the excellent ORR/OER electrocatalysis activities with  $E_{1/2} = 0.89$  V,  $E_{10} = 1.68$ , and  $\Delta E = 0.79$  V in 0.1 M KOH (Figure 11d), were systematically studied by DFT calculations. As illustrated in the theoretical ORR and OER volcano plots, the N-doped defect A7 site was identified as the most active for ORR, and the dopant-free carbon defect A6 showed the highest OER activity (Figure 11e). In a recent study, the oxygen-induced vacancies in an N-doped nanocarbon were claimed critical for improving the ORR activity of the air electrode.<sup>[93]</sup> Combined DFT calculations and experimental studies suggested that the oxygen-induced vacancies can deliver better ORR activity than bare nitrogen doping in the basal plane. The rechargeable ZABs assembled with this catalyst showed an excellent

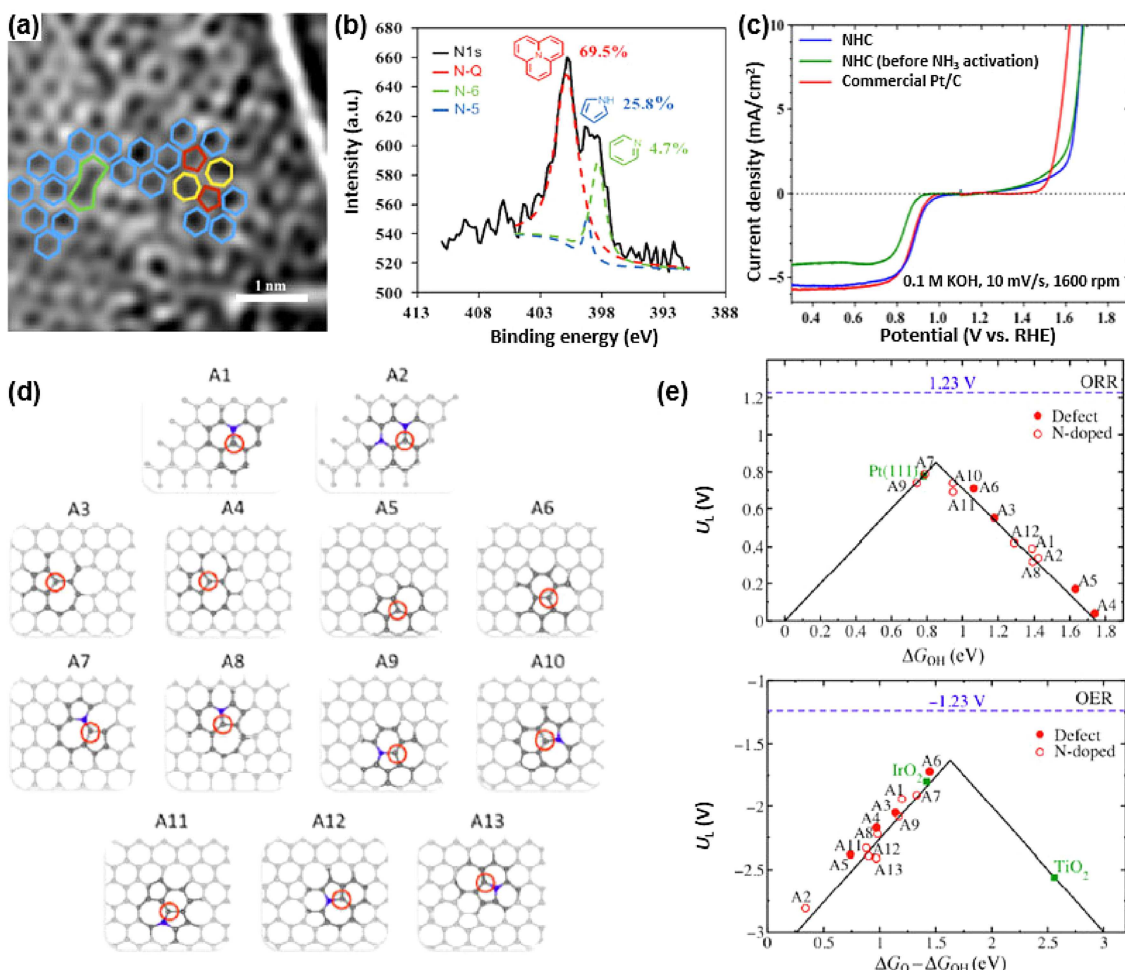


**Figure 11.** Experimental and theoretical studies on the NHC catalyst. a) HR-TEM image of the NHC highlighting the defects for better visualization. b) HR-X-ray photoelectron spectroscopy (XPS) spectra of N 1s in the NHC. c) Examined configurations of active sites. d) LSV plots of the ORR and OER for different catalysts in 0.1 M KOH (scan rate 10 mVs<sup>-1</sup>). e) ORR and OER volcano plots as a function of  $\Delta G_{OH}$  and  $\Delta G_O - \Delta G_{OH}$ , respectively. Reproduced with permission.<sup>[86]</sup> Copyright 2017, Springer Nature.

performance, including high power density (186.3 mW cm<sup>-2</sup>) and stable cycling performance over long-term operation.

Porous B, N co-doped nanocarbon (B, N-carbon) with rationally engineered defects has been prepared with enhanced catalytic performance using a sacrificial template method (Figure 12a–c).<sup>[89]</sup> Ethyl cellulose (EC, carbon precursor) and 4-(1-naphthyl)benzeneboronic acid (NBBA, boron precursor) were precipitated on the surface of a Zn-based template, followed with pyrolysis in NH<sub>3</sub> at 800 °C and acid leaching, to produce finely graphitic B, N-carbon. The abundant carbon defects (e.g., topological defects on the corners, edge defects on the broken fringes, Figure 12d, e) are generated from the decomposition of the uniformly dispersed oxygen species in EC, which can facilitate the activation of the graphitic π-electron system and O<sub>2</sub> chemisorption.<sup>[94]</sup> Together with B, N dopants that synergistically modulates the charge density of the adjacent carbon, the defect-rich B, N-carbons possess abundant active sites and excellent oxygen catalytic activity ( $\Delta E = 0.71$  V, Figure 12f). ZABs using this air electrode outperformed those using Pt/C + RuO<sub>2</sub>, as evidenced with a lower

charge-discharge voltage gap, lower internal electric resistance, and better stability (Figure 12g).

Similarly, N, B co-doped and defect-rich graphitic carbon nanocages (NB-CNs) were prepared by rationally balancing the heteroatom doping and defect engineering.<sup>[88]</sup> This material is rich in carbon defects, e.g., topological disclinations at the corner, surficial broken fringes, and micropores (Figure 12h). DFT calculations reveal that the best ORR/OER performance is from the configuration with B *meta* to a pyridinic-N (4 in Figure 12i). B atom serves as the optimal ORR active site with the lowest overpotential of 0.34 V and the neighboring carbon as the OER active site (3 in Figure 12i) with the minimum overpotential of 0.39 V. The NB-CN showed excellent bifunctional activities with the  $\Delta E$  of 0.82 V (Figure 12j). A primary ZAB using the NB-CN as the air electrode possessed an open circuit voltage of 1.4 V, with a peak power density of ~320 mW cm<sup>-2</sup>, comparable to that with Pt/C electrode. Through rational design to balance the heteroatom doping and defect engineering, desired active sites with regulated electronic configuration can be generated in the nanostructured carbon, contributing to improved catalytic activities.

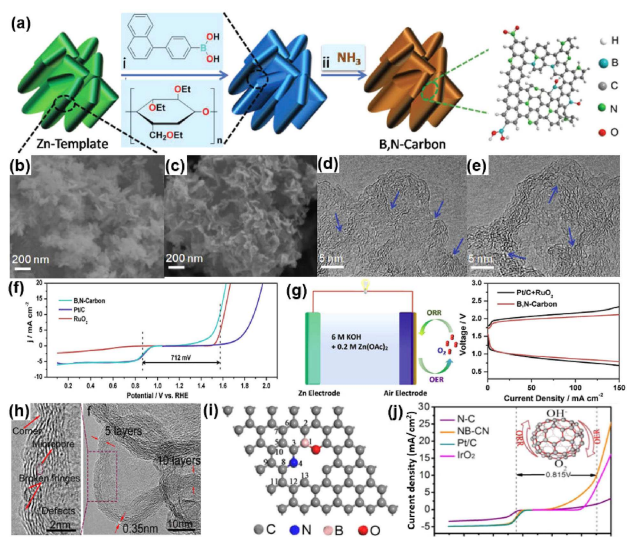


**Figure 12.** B, N co-doped and defect-rich nanocarbons as ORR and OER bifunctional electrocatalysts. a) Schematic illustration of the preparation process for B, N-carbon. b, c) SEM images of the Zn-based template and B, N-carbon. d, e) HR-TEM images of B, N-carbon with arrows indicating the defects. f) Bifunctional catalytic activities for ORR and OER in  $O_2$ -saturated 1.0 M KOH. g) Illustration of the ZAB and the charge-discharge polarization curves of two-electrode rechargeable ZABs. Reproduced with permission.<sup>[89]</sup> Copyright 2018, Wiley-VCH. h) HR-TEM images of NB-CN. i) Relative position of N, B and O for the N, B co-doped graphene considered in the DFT calculations. j) LSV curves of different catalysts at 1600 rpm in 0.1 M KOH (scan rate: 5 mV s<sup>-1</sup>). Reproduced with permission.<sup>[88]</sup> Copyright 2017, Elsevier.

### 3.3. Hybrid Carbon Nanostructures

Heteroatom doping and defect engineering can effectively increase the electroactivity of nanocarbon materials, yet side effects may come along, especially the deteriorated electrical conductivity. Hybridizing various carbon nanostructures provides a prospective way to further improve the electrocatalytic performance through multiple effects, such as providing more accessible active sites and increasing the electrical conductivity.<sup>[44–45]</sup> For instance, an ultrathin N-doped holey carbon layer (HLC) was grown on a graphene nanosheet (N-HC@G) to provide abundant active sites without destroying the  $sp^2$  conjugated structure.<sup>[95]</sup> Pyridinic-N was selectively doped on the edge sites of HCLs for high catalytic activity; while the sandwiched graphene sheets acted as a mechanical support to stabilize the HCL and promote charge transfer. Consequently, the N-HC@G exhibited outstanding ORR and OER activities in both alkaline and acidic media (Figure 13a–c).

More importantly, by coupling the active species with highly conductive supports, free-standing and light-weight air electrodes can be achieved with high specific energy density. Zhang and co-workers prepared a self-standing carbon paper composed of defect-rich, N doped carbon fiber wrapped with in situ exfoliated graphene nanosheets (DN-CP@G). The DN-CP@G has a core-shell structure with defect-rich graphene oxide nanosheets (GNS) as the outer layer and graphitic carbon (GC) fibers as the inner core (Figure 13d, e).<sup>[96]</sup> As illustrated in Figure 13f, the GNS possesses abundant defective sites, which

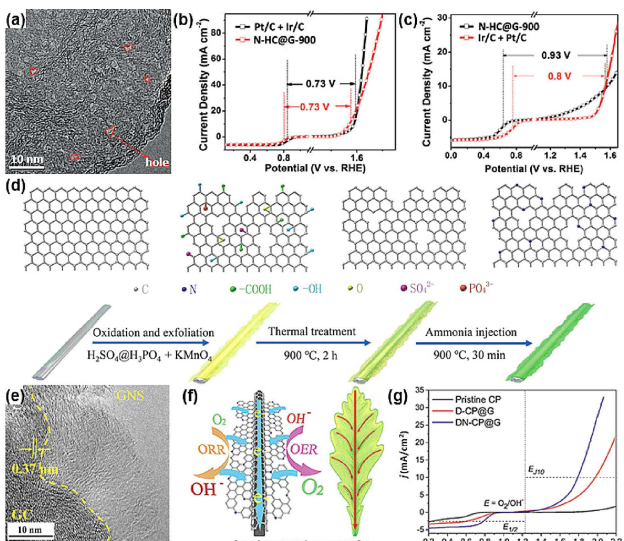


**Figure 13.** Coupled carbon nanostructures for bifunctional oxygen catalysis. a) HR-TEM image of N-HC@G. b) LSV curves of N-HC@G in 1 M KOH. c) LSV curves of N-HC@G in 0.5 M  $H_2SO_4$ . Reproduced with permission.<sup>[95]</sup> Copyright 2018, Wiley-VCH. d) Schematic illustration of the synthesis of DN-CP@G. e) HR-TEM image indicating the in situ exfoliated graphene nanosheets (GNS) on graphitic carbon (GC) fibers. The enlarged lattice fringes indicate defective sites. f) Schematic representation of strongly coupled core-shell structure for bifunctional ORR and OER. g) LSV curves of different catalysts in 0.1 M KOH. Reproduced with permission.<sup>[96]</sup> Copyright 2018, Wiley-VCH.

effectively modulate the charge/spin distribution in the carbon matrix, enabling a high electrocatalytic activity. While the GC inner layer preserves its high conductivity, facilitating fast electron (Figure 13g). Lai and co-workers prepared free-standing N-doped vertically-aligned CNTs (N-VA-CNTs) supported on graphene foam (GF) as air-breathing electrodes for rechargeable ZABs.<sup>[97]</sup> The N-VA-CNTs worked as efficient oxygen electrocatalysts and provided appropriate channels for ion and gas diffusion. Consequently, the N-VA-CNTs/GF could be used as a free-standing and light-weight air-cathode with highly integrated structure for high-performance electrocatalysts and gas diffusion layer for ZABs.

## 4. Carbon-Based Composites

Carbon nanomaterials usually possess high conductivity and large specific surface area. Moreover, they can be easily fabricated into various nanostructures and thus generally considered ideal supports for metals, metal oxides, and other compounds for efficient oxygen catalysis. In this section, recent advances in related topics are summarized.

### 4.1. Carbon-Metal Composites

Nanostructured carbon supported transition metal atoms or metal alloys nanoparticles have been widely explored for ORR and OER electrocatalysis.<sup>[74,98–119]</sup> As above mentioned, heteroatoms, such as N, can be incorporated into carbon frame-

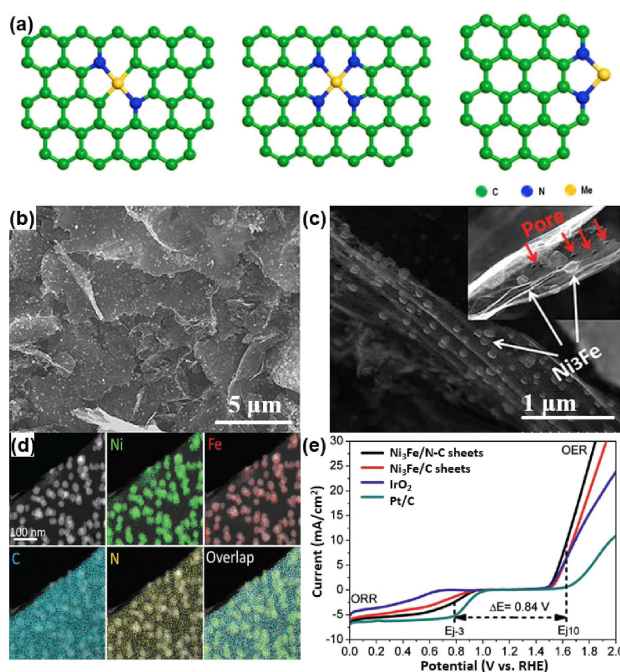


**Figure 14.** a) General molecular structures of the M–N–C material. Reproduced with permission.<sup>[29]</sup> Copyright 2017, American Chemical Society. B–c) SEM images of Ni<sub>3</sub>Fe/N–C (white and red arrows reveal the uniform distribution of Ni<sub>3</sub>Fe particles and nanopores, respectively). d) STEM image and corresponding elemental mappings. e) Overall polarization curves for Ni<sub>3</sub>Fe/N–C sheets, Ni<sub>3</sub>Fe/C sheets, IrO<sub>2</sub>, and Pt/C catalysts within the ORR and OER potential window. Reproduced with permission.<sup>[98]</sup> Copyright 2017, Wiley-VCH.

works for enhanced electrocatalytic activity through electron modulation. Moreover, these dopants can further serve as the anchoring centres to accommodate metal atoms or metal alloys particles through the strong coupling effects, forming electrocatalytically active and stable M–N–C moieties (Figure 14a).<sup>[29,120]</sup> Usually, M–N–C catalysts are achieved by the pyrolysis of precursors containing metal, nitrogen, and carbon.<sup>[121]</sup> Proper selection of precursors and rational design of the synthetic route can produce better-performing electrocatalysts.<sup>[29,121–123]</sup>

Among them, Fe, Co, Ni, and their alloys have attracted growing research interest for ZAB applications and been extensively investigated by experimental and theoretical studies.<sup>[99–105,124–127]</sup> For instance, Ni<sub>3</sub>Fe nanoparticles embedded in N-doped 2D porous graphitic carbon (Ni<sub>3</sub>Fe/N–C) sheets have been obtained through a pyrolysis-based approach.<sup>[98]</sup> Ni<sub>3</sub>Fe particles are well dispersed on carbon sheets with a homogeneous distribution of Ni, Fe, and N elements over the carbon sheets (Figure 14b–d). As a result, the Ni<sub>3</sub>Fe/N–C sheets exhibited high bifunctional ORR and OER activity and stability with a small  $\Delta E$  of 0.84 V (Figure 14e).

Metal-organic frameworks (MOFs), especially the zeolite imidazole frameworks (ZIFs), have been extensively studied as self-sacrificial templates to fabricate bifunctional oxygen catalysts with prominent performance due to their highly ordered cavities, open channels, tuneable composition, and versatile structures.<sup>[74,106–118,128–134]</sup> Qiu and co-workers reported double-shelled hybrid nanocages (DSNCs) with superior bifunctional

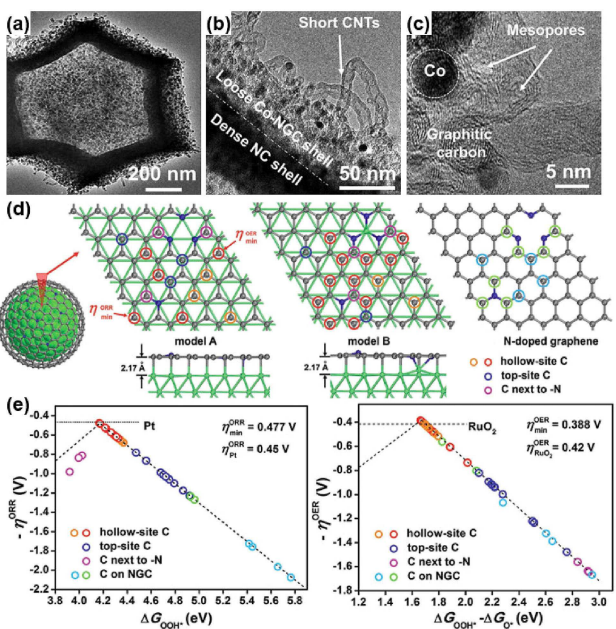


**Figure 15.** MOF-derived hybrid carbon nanocages as bifunctional oxygen catalysts. A–c) TEM images revealing the core-shell structure of NC@Co-NGC DSNCs. d) Overall polarization curves of different catalysts in O<sub>2</sub>-saturated 0.1 M KOH. e) Schematic illustration of the models of Co-NGC and N-doped graphene for DFT calculations. The Co, C, and N atoms are shown in green, gray, and blue color, respectively. Reproduced with permission.<sup>[109]</sup> Copyright 2017, Wiley-VCH

catalytic properties derived from self-templating core-shell ZIF-8@ZIF-67.<sup>[109]</sup> The DSNCs are composed of a ZIF-8-derived inner shell of N-doped mesoporous graphitic carbon (NC), which facilitates the diffusion kinetics; and a ZIF-67-derived outer shell of Co–N-doped graphitic carbon (Co-NGC) that is highly active for both ORR and OER (Figure 15a–c). Based on a simplified model of N-doped graphene monolayer adsorbed on the (111) surface of the face centred cubic Co crystal (Figure 15d), DFT calculations revealed that the high activity of Co-NGC arose from the strong yet favourable adsorption of OOH\* on the uncoordinated hollow-site C atoms. Moreover, the active C sites *para* to doped graphitic-type and pyridinic-type N atoms exhibited the highest activity towards ORR and OER (Figure 15e, f), respectively. As such, the DSNCs nanocages exhibited an excellent electrocatalytic activity and durability for ORR and OER with  $E_{1/2} = 0.82$  V,  $E_{10} = 1.64$  V, and  $\Delta E = 0.82$  V, respectively. Apart from this, other MOF-derived M–N–C materials can also be easily fabricated into various open porous nanostructures for full utilization of the high catalytic activity, such as 1D nanofibers,<sup>[116–117]</sup> 2D nanoflakes,<sup>[129]</sup> and 3D frameworks.<sup>[115,130–134]</sup>

Carbon–metal/metal alloy composites can also be fabricated by annealing the electro-spun fiber precursors. The electro-spinning process allows the rational design and precise control over the composition and structure of the fiber precursor, which provides a facile method to decorate metal nanoparticles and heteroatoms on the obtained carbon for bifunctional catalysis. For instance, NiCo alloy nanoparticles decorated on N-doped carbon nanofibers (NiCo@N–C) was prepared using a

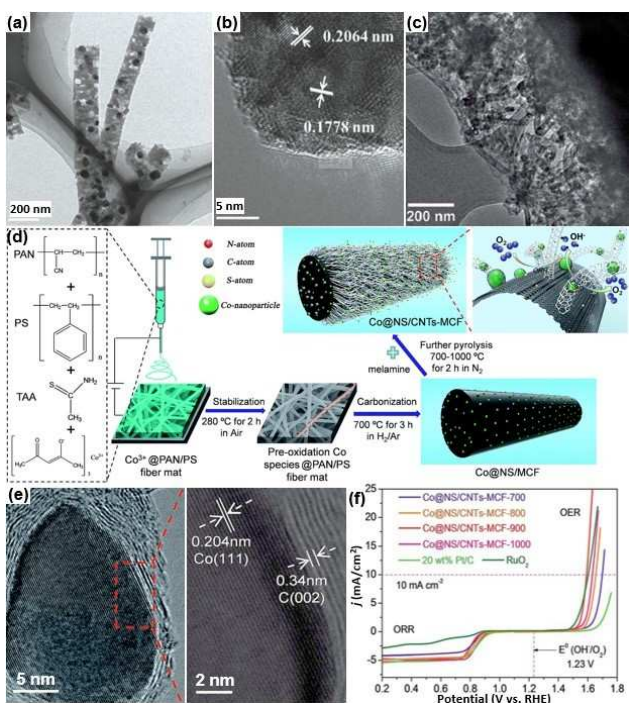


**Figure 16.** Electro-spun fiber derived carbon-metal/metal alloy composites for bifunctional oxygen catalysis. a) TEM and b) HR-TEM images of NiCo@N-C. The lattice fringes of 0.2064 nm and 0.1778 nm are related to the (111) and (200) lattice planes in metallic Ni and Co, respectively. Reproduced with permission.<sup>[100]</sup> Copyright 2018, Wiley-VCH. c) TEM image of Co@CNT-MCF. d) Schematic illustration of the preparation process for Co@CNT-MCF mats. e) HR-TEM images of Co@CNT-MCF. f) Overall oxygen electrode activities of various catalysts in  $O_2$ -saturated 0.1 M KOH (scan rate: 5 mV s<sup>-1</sup>). Reproduced with permission.<sup>[135]</sup> Copyright 2017, The Royal Society of Chemistry.

facile electrospinning method and post-calcination treatment (Figure 16a, b). The NiCo@N-C exhibited an outstanding ORR ( $E_{1/2}=0.80$  V) and OER ( $E_{10}=1.76$  V) electrochemical performance due to the synergistic effects between the NiCo alloy and N-doped carbon. Similarly, Co nanoparticles anchored on carbon nanotube-grafted and N, S co-doped multichannel carbon fibers (Co@NS/CNT-MCFs) were reported (Figure 16c–e).<sup>[135]</sup> The metallic Co nanoparticles not only served as catalytic active sites combined with N, S dual dopants but also catalysed the growth of grafted CNTs on the MCFs, which facilitated the electron and mass transfer during the electrocatalytic reaction. All these features contributed to excellent bifunctional ORR and OER catalytic activities of Co@NS/CNT-MCFs (Figure 16f).

Recently, carbon-metal composites with atomically distributed active sites have attracted growing interest to achieve enhanced catalytic activity *via* the maximized atomic utilization and a greater number of active sites as well as to gain an in-depth understanding of the catalytic mechanisms.<sup>[136–147]</sup> Zhang and co-workers prepared Co/N/O tri-doped graphene mesh (NGM-Co) containing atomically dispersed Co-N<sub>x</sub> active sites by defect engineering (Figure 17a, b).<sup>[136]</sup> The Co-N<sub>x</sub> moieties can cause decreased electron density of the adjacent C atoms due to the strong electron-withdrawing effect, which facilitates the adsorption of ORR/OER intermediates and promotes the electron transfer for enhanced kinetics, resulting in good ORR/

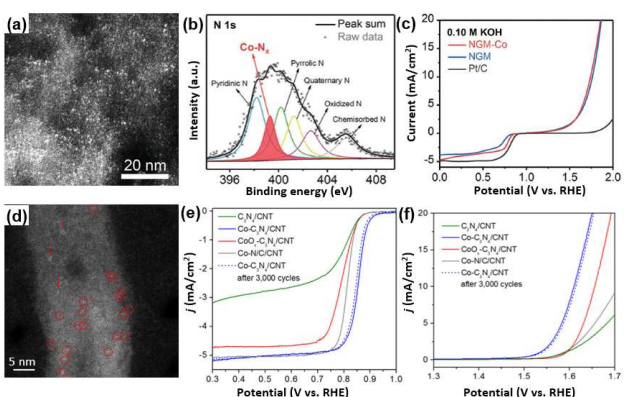


**Figure 17.** Carbon-metal composites with atomically dispersed active sites. a) Dark-field HR-TEM image showing highly dispersed Co atoms in graphene layers. b) XPS spectra of N 1s indicating the formation of Co-N<sub>x</sub>C configurations. c) LSV curves of different catalysts showing the bifunctional ORR/OER catalytic activity (scan rate 10.0 mV s<sup>-1</sup>). Reproduced with permission.<sup>[136]</sup> Copyright 2017, Wiley-VCH. d) HAADF-STEM image of Co-C<sub>3</sub>N<sub>4</sub>/CNT. Circles and arrows indicate single Co atoms and Co clusters, respectively. e) ORR and f) OER polarization curves of different Co based catalysts. Reproduced with permission.<sup>[137]</sup> Copyright 2017, American Chemical Society.

OER bifunctional activities (Figure 17c). Qiao et al. prepared a Co-C<sub>3</sub>N<sub>4</sub> complex supported on multi-walled carbon nanotubes (Co-C<sub>3</sub>N<sub>4</sub>/CNT, Figure 17d) with precise Co-N<sub>2</sub> coordination.<sup>[137]</sup> DFT calculations and experimental studies revealed that the Co-N<sub>2</sub> moiety served as the main active site and exhibited good stability for the reversible bifunctional oxygen catalysis, as evidenced by the minuscule performance attenuation after 3000 cycles (Figure 17e, f). In their recent work, Han et al. reported the spatial isolation of Co species on the atomic scale by tuning the Zn dopant content in predesigned bimetallic ZnCo-ZIFs.<sup>[148]</sup> The isolated Co atoms exhibited high reactivity and stability, leading to superior bifunctional ORR/OER activity ( $\Delta E=0.98$  V), durability, and reversibility of the single-atom Co catalysts in ZABs. The ZAB with single-atom Co catalysts delivered the highest open circuit potential (~1.46 V) and the highest power density (105.3 mW cm<sup>-2</sup> at 158 mA cm<sup>-2</sup>) in the investigated catalysts, approaching that of Pt/C (110.4 mW cm<sup>-2</sup> at 184 mA cm<sup>-2</sup>).

In general, the electrocatalytic activity of carbon-metal composites is attributed to the strong coupling between metal and carbon materials (e.g., the formation of highly active M–N–C moieties), which can effectively modify the local electronic structure and therefore optimize the intermediate adsorption.<sup>[130,142,149–151]</sup> Nonetheless, direct evidence of metal participation in the M–N–C system has so far been lacking, due to the complexity of various nanostructures and metal coordination compositions.<sup>[152]</sup> Conclusive identification of the nature of the active sites still requires further efforts with the combination of theoretical simulations, advanced characterization techniques, and controllable fabrication of targeted active sites at atomic precision.

## 4.2. Carbon-Metal Oxide Composites

Metal oxides, including Mn, Co, Ni, and Fe oxides, are considered feasible for bifunctional oxygen catalysis because of their intrinsic activity, low cost, environmental friendliness, earth abundance, and structural flexibility.<sup>[35,153–157]</sup> For instance, manganese oxides ( $\text{MnO}_x$ ) can be obtained in the form of  $\text{Mn}_5\text{O}_8$ ,  $\text{Mn}_3\text{O}_4$ ,  $\text{Mn}_2\text{O}_3$ ,  $\text{MnO}_2$ ,  $\text{MnO}$ ,  $\text{MnOOH}$ , etc., as well as in various morphologies (e.g., urchin-like,<sup>[158]</sup> star-like,<sup>[159]</sup> nanoballs,<sup>[160]</sup> nanowires,<sup>[161–163]</sup> nanorods,<sup>[164–165]</sup> nanotubes,<sup>[166–169]</sup> nanosheets,<sup>[170–173]</sup> nanoflowers,<sup>[174–175]</sup> and hollow spheres,<sup>[176–177]</sup> as shown in Figure 18), which all show considerable catalytic activities in alkaline media.<sup>[157,178]</sup> Such compositional and structural flexibility of metal oxides provides a great opportunity to regulate their electrocatalytic performances. It has been reported that the catalytic activity of polymorphic  $\text{MnO}_2$  is in the sequence of  $\beta\text{-MnO}_2 < \lambda\text{-MnO}_2 < \gamma\text{-MnO}_2 < \alpha\text{-MnO}_2 \sim \delta\text{-MnO}_2$ , due to crystallographic orientation related  $\text{O}_2$  dissociation.<sup>[157,179]</sup>

However, metal oxides usually suffer from poor electrical conductivity and limited specific surface area, because of the self-agglomeration induced by the high temperature anneal during their fabrication, which hinder their applications for oxygen catalysis. Integration of metal oxides with nanostructured carbon supports, which can provide an efficient conductive network and accessible surface area to facilitate the

electron transfer and mass diffusion during ORR and OER, provides a perspective way to further improve electrocatalytic performances. Moreover, it is generally believed that a synergistic effect can be generated between the metal oxides and heteroatom dopants in nanocarbons, contributing to enhanced electrocatalytic performances.<sup>[180–188]</sup>

Guan et al. reported a bifunctional oxygen catalyst composed of hollow  $\text{Co}_3\text{O}_4$  nanospheres embedded in N-doped carbon nanowall arrays on flexible carbon cloth (NC– $\text{Co}_3\text{O}_4/\text{CC}$ ) with high electrocatalytic activity and enhanced durability.<sup>[182]</sup> The irregular shape of the hollow  $\text{Co}_3\text{O}_4$  nanospheres was caused by the nanoscale Kirkendall effect between the carbon-metal interface,<sup>[189]</sup> which presents a high density of defects (steps and grain boundaries). These defects endow sufficient active sites with short ion-diffusion length, while the N-doped carbon coverage layers provide high electrical conductivity and enhanced stability. As a result, a ZAB using this NC– $\text{Co}_3\text{O}_4/\text{CC}$  material as the flexible air cathode delivered a high open circuit potential of 1.44 V, a capacity of 387.2 mAh g<sup>-1</sup>, and excellent cycling stability. Zhong et al. prepared a mesoporous  $\text{Co}_3\text{O}_4/\text{N-rGO}$  hybrid nanosheet composed of  $\text{Co}_3\text{O}_4$  atomic layers strongly coupled with N-doped rGO as high-performance bifunctional catalysts for knittable fiber-shaped ZABs.<sup>[184]</sup> Benefiting from the high surface area, large pore volume, and the strong synergistic effect between  $\text{Co}_3\text{O}_4$  and N-rGO, the catalyst exhibited high activity and superior durability for both ORR and OER, enabling high-performance fiber-shaped ZABs with a high volumetric energy density (36.1 mWh cm<sup>-3</sup>).

Metal oxides can be further modified with a secondary metal/metal oxides to manipulate the inherent electronic and/or surface structures of the host material for improved electrochemical activity.<sup>[192–194]</sup> For this purpose, Yin et al. prepared the MO–Co@N-doped carbons (NC, M=Zn or Co) by the pyrolysis of bimetal CoZn containing MOFs as bifunctional oxygen catalysts for ZABs.<sup>[190]</sup> In this bimetal MOF, Zn is highly volatile at high temperature and can be evaporated during the pyrolysis, resulting in improved spatial dispersion of the remaining metal species in the NC matrices and greatly affecting the compositions and the local nanostructures of the resulted catalysts.<sup>[144]</sup> As illustrated in Figure 19a, the optimized ZnCo-NC-700 contains nearly mono-dispersed Co@ZnO core-shell nanostructures totally coated with highly graphitic NC, as well as well-developed multi-walled CNTs, which facilitates the charge transfer during the electrocatalytic processes. Moreover, Zn in the MOF precursor can also lead to enhanced surface contents of Co-N<sub>x</sub> and Co<sup>3+</sup>/Co<sup>2+</sup> ratios for OER and surface contents of pyridinic N for ORR (Figure 19b, c), contributing to improved bifunctional oxygen electrocatalysis.

Besides, Lee and co-workers developed another highly efficient bifunctional Ni-MnO/rGO catalyst with active MnO for ORR and metallic Ni for OER with the assistance of the 3D porous rGO aerogels (Figure 19d–f).<sup>[191]</sup> The 3D porous rGO aerogels are not only favourable for the transport of liquid electrolyte, oxygen, and electron but also guarantee the efficient immobilization of metal particles, contributing to outstanding oxygen electrocatalytic activity a  $\Delta E$  of 0.82 V as well as good stability (Figure 19g). This material thus endowed

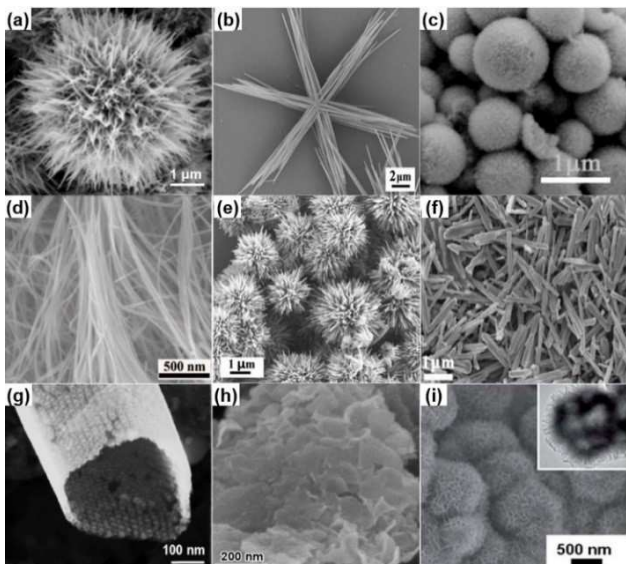


**Figure 18.** SEM images of  $\text{MnO}_x$  in various morphologies. a) Urchin-like  $\alpha\text{-MnO}_2$ . Reproduced with permission.<sup>[158]</sup> Copyright 2015, Elsevier. b) Star-like  $\epsilon\text{-MnO}_2$ . Reproduced with permission.<sup>[159]</sup> Copyright 2016, The Royal Society of Chemistry. c) Porous  $\text{Mn}_2\text{O}_3$  nanoballs. Reproduced with permission.<sup>[160]</sup> Copyright 2016, The Royal Society of Chemistry. d)  $\text{MnO}_2$  nanowires. Reproduced with permission.<sup>[162]</sup> Copyright 2009, American Chemical Society. e) Dandelion-like  $\alpha\text{-MnO}_2$  nanoflowers. Reproduced with permission.<sup>[174]</sup> Copyright 2017, Elsevier. f)  $\beta\text{-MnO}_2$  nanorods. Reproduced with permission.<sup>[165]</sup> Copyright 2015, Wiley-VCH. g)  $\text{Mn}_3\text{O}_4$  nanotubes. Reproduced with permission.<sup>[166]</sup> Copyright 2017, American Chemical Society. h) Nanoporous  $\text{MnO}_2$  nanosheets. Reproduced with permission.<sup>[170]</sup> Copyright 2018, Wiley-VCH. i) Fe-containing  $\gamma\text{-MnO}_2$  hollow microspheres. Reproduced with permission.<sup>[176]</sup> Copyright 2016, The Royal Society of Chemistry.

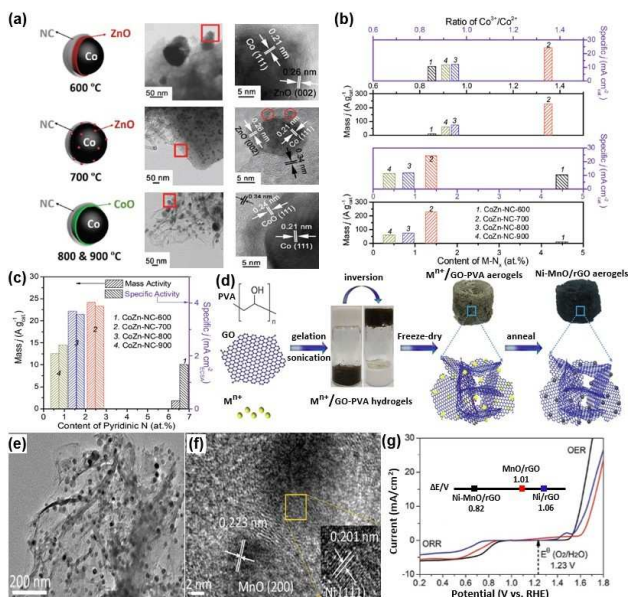


**Figure 19.** a) Schematic illustration and corresponding TEM images of ZnCo-NC-T ( $T=600, 700, 800$ , representing the pyrolysis temperature). b) Relationship between the OER mass and specific activity and the surface content of  $M-N_x$  and ratio of  $Co^{3+}/Co^{2+}$ . c) Relationship between the ORR mass and specific activity and the surface content of pyridinic N. Reproduced with permission.<sup>[190]</sup> Copyright 2017, Wiley-VCH. d) Schematic illustration of the preparation of Ni-MnO/rGO aerogels. e, f) TEM and HR-TEM images of Ni-MnO/rGO aerogels. g) Overall polarization curves of catalysts within the ORR and OER potential window (rotation rate: 1600 rpm, sweep rate: 5 mV s<sup>-1</sup>); inset shows the value of  $\Delta E$  for catalysts. Reproduced with permission.<sup>[191]</sup> Copyright 2018, Wiley-VCH.

the ZABs with longer cycling life and higher voltaic efficiency that outperformed the state-of-the-art Pt/C + RuO<sub>2</sub>-driven battery. Wu and co-workers supported cobalt-manganese oxides on N-doped carbon nanotubes (NCNT/Co<sub>x</sub>Mn<sub>1-x</sub>O) as an oxygen catalyst for rechargeable ZABs.<sup>[195]</sup> A rechargeable ZAB using the NCNT/Co<sub>x</sub>Mn<sub>1-x</sub>O as the air electrode catalyst possessed a low charge-discharge gap of 0.57 V and high stability, which is attributed to that highly graphitic CNTs can mitigate carbon oxidation and increase the corrosion resistance.

Recently, spinel oxides ( $A_xB_{3-x}O_4$ ) and perovskite oxides ( $ABO_3$ ) have been widely investigated as bifunctional oxygen catalysts. In the spinel structure, the coexistence of tetrahedral and octahedra sites can accommodate different metal cations with a wide range of valence states to deliver promising ORR and OER activities (Figure 20a). Especially when supported on N-doped carbon materials (e.g. carbon nanotubes), the interaction between bimetal atoms and N dopants can generate synergistic effects and yield superior catalytic activities.<sup>[196–198]</sup> Schuhmann et al. developed a facile thermal oxidative treatment method to convert the residual Co and Mn oxide nanoparticles buried inside the N-doped CNTs to spinel Mn-Co oxide nanoparticles partially embedded in the N-doped CNTs.<sup>[199]</sup> The resulted catalysts showed excellent bifunctional ORR and OER performance, as a result of the intimate contact between the Mn-Co spinel oxide and the graphitic walls of CNTs. Li and co-workers prepared an all-in-one bifunctional oxygen electrode film by adhering NiCoO<sub>4</sub> nanosheets to N, O

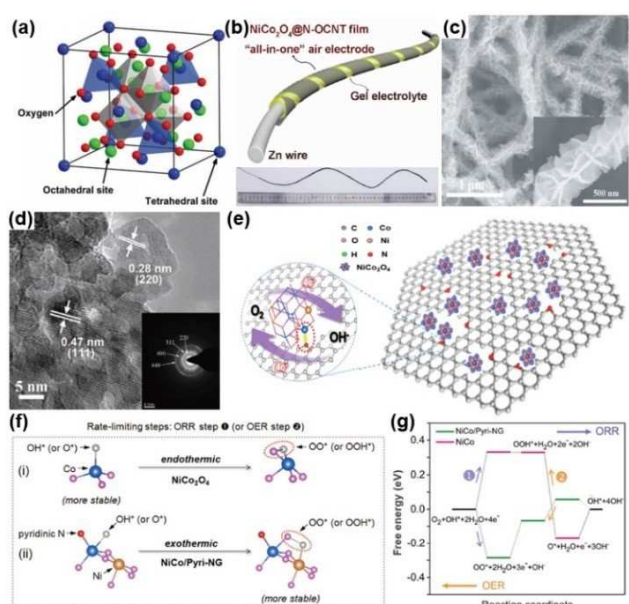


**Figure 20.** a) Spinel crystal structure. Reproduced with permission.<sup>[154]</sup> Copyright 2017, Wiley-VCH. b) Schematic illustration of flexible ZAB utilizing the all-in-one NiCo<sub>2</sub>O<sub>4</sub>@N-OCNT as air electrode and the optical image of a ~50 cm long cable-like flexible ZAB. c) SEM image of NiCo<sub>2</sub>O<sub>4</sub>@N-OCNT film showing NiCo<sub>2</sub>O<sub>4</sub> nanoflower wrapping CNT interconnected network. d) HR-TEM image and selected-area electron diffraction image (inset figure) indicating the formation of NiCo<sub>2</sub>O<sub>4</sub> polycrystalline nanoflakes. Reproduced with permission.<sup>[200]</sup> Copyright 2018, Wiley-VCH. e) Schematic illustration of NiCo<sub>2</sub>O<sub>4</sub>/N-doped graphene (NiCo<sub>2</sub>O<sub>4</sub>/NLG) hybrids. f) Adsorption configurations of oxygen-containing species on the Co site of NiCo<sub>2</sub>O<sub>4</sub> (i) and NiCo<sub>2</sub>O<sub>4</sub>/Pyri-NG (ii) for the ORR/OER rate-limiting steps. g) Free energy diagram of ORR and OER processes on NiCo<sub>2</sub>O<sub>4</sub>/Pyri-NG composite and plain NiCo<sub>2</sub>O<sub>4</sub> nanoparticle. Reproduced with permission.<sup>[201]</sup> Copyright 2018, Wiley-VCH.

co-doped CNT films (NiCo<sub>2</sub>O<sub>4</sub>@N-OCNT), and used it as a freestanding air electrode for a cable-like ZAB

(Figure 20b).<sup>[200]</sup> The NiCo<sub>2</sub>O<sub>4</sub>@N-OCNT catalyst is composed of porous nanosheets, which were constructed by a large number of secondary polycrystalline NiCo<sub>2</sub>O<sub>4</sub> nanoflakes homogeneously grown around the CNT bundles (Figure 20c, d). The composite films exhibited excellent reversible oxygen catalytic performance, with low Tafel slopes for ORR (50 mV dec<sup>-1</sup>) and OER (92 mV dec<sup>-1</sup>). The flexible and cable-like ZABs with this catalyst possessed a high operating potential (~1.2 V at 0.25 mA cm<sup>-2</sup>), low charging-discharging overpotential (~0.7 V), and stable cycling performance.

To identify the origin of the high bifunctional oxygen catalytic performance of the hybrid catalysts composed of spinel oxides and heteroatom-doped carbon, Wang et al. developed low-intensity pulsed-laser irradiation (LI-PLI) method to clarify the contributions from different M-N<sub>x</sub> configurations to the synergistic effect.<sup>[201]</sup> The LI-PLI method enables the controllable tuning of the in-plane mesopores density of the resulted mesoporous GO,

thus facilitating the engineering of the relative concentrations of the pyridinic and pyrrolic N in the obtained NiCo<sub>2</sub>O<sub>4</sub>/NLG catalyst (Figure 20e). DFT calculations revealed that the synergistic effect between pyridinic N, surface Co, and its neighboring Ni contributes most to the enhanced reversible

oxygen electrocatalysis. In the ORR/OER rate-limiting steps, the  $\text{OO}^*$  (ORR) and  $\text{OOH}^*$  (OER) species can co-adsorb on the Co site and its adjacent Ni site in  $\text{NiCo}_2\text{O}_4/\text{Pyri-NG}$  (Figure 20f), lowering the overpotential for reversible oxygen electrocatalysis (Figure 20g). Furthermore, the pyridinic-N-Co configuration can also facilitate the electron storage and transfer, which enables the adsorbed oxygen-containing species ( $\text{O}^*$ ,  $\text{OH}^*$ ,  $\text{OO}^*$ ,  $\text{OOH}^*$ ) on the active sites to obtain electrons from both Co and pyridinic N, leading to optimized adsorption of the intermediates and facile ORR/OER processes. Consequently, this  $\text{NiCo}_2\text{O}_4/\text{NLG}$  catalyst exhibited superior bifunctional ORR/OER capability ( $\Delta E=0.75$  V) and delivered a high open circuit voltage of nearly 1.49 V and a low discharge/charge overpotential of 0.8 V, when used for rechargeable ZABs.

Compared with spinel oxides, the perovskite oxides, with a general formula of  $\text{ABO}_3$ , are more stable and corrosion resistant.<sup>[35]</sup> Figure 21a presents an ideal cubic-symmetry perovskite structure. The larger A-site cation is commonly a rare-earth or alkaline earth metal, and the smaller B-site cation is commonly a transition metal, which mainly contributes to the ORR/OER activities. The d-orbitals of the transition metal cations split into the low-lying  $t_{2g}$  orbitals and the high-lying  $e_g$  orbitals. The  $e_g$  orbital participates in the formation of  $\sigma$ -bonding with a surface adsorbate, and its occupancy can greatly influence the binding of oxygen-related intermediates on B-site to provide ORR/OER activities. Shao-Horn et al. used the  $e_g$  occupation of the B-site transition metal as a descriptor to predict the ORR and OER activity of different types of perovskites.<sup>[10,202]</sup> They found that the extent of B-site transition-metal-oxygen covalency served as a secondary ORR activity descriptor.<sup>[10]</sup> The volcano plots of the ORR and OER against the  $e_g$  occupancy in perovskite-based oxides are shown in Fig-

ure 21b, c. It can be clearly seen that the perovskites with near-unity occupancy of the  $e_g$  orbital, such as  $\text{LaMnO}_3$  ( $e_g \approx 1$ ) and  $\text{Ba}_{0.5}\text{Sr}_{0.5}\text{Co}_{0.8}\text{Fe}_{0.2}\text{O}_{3-\delta}$  (BSCF,  $e_g \approx 1.2$ ), exhibited the highest ORR and OER activity, respectively. Other electronic structure factors of B-site transition metal (e.g., number of d electrons,<sup>[204]</sup> charge-transfer energy,<sup>[205]</sup> and oxidation state<sup>[206]</sup>) have also been reported to affect the ORR/OER activity, indicating a prospective way to develop highly active ORR/OER bifunctional catalysts by rationally tailoring the electronic structures of B-site transition metals in perovskites.<sup>[206–213]</sup>

Coupling perovskites with carbon can help overcome their intrinsic shortage of the electrical conductivity, resulting in enhanced electrochemical performance.<sup>[203,214–219]</sup> For instance, the  $\text{Ba}_{0.5}\text{Sr}_{0.5}\text{Co}_{0.8}\text{Fe}_{0.2}\text{O}_{3-\delta}$  (BSCF) modified with acetylene black (BSCF/AB) exhibited significantly higher ORR/OER activity than the pristine BSCF catalyst (Figure 21d), which is attributed to the enhanced electrical conductivity and the altered oxidation state of Co by carbon.<sup>[203]</sup> Kwak et al. reported a multifunctional P-3D catalyst consisting of  $(\text{PrBa}_{0.5}\text{Sr}_{0.5})_{0.95}\text{Co}_{1.5}\text{Fe}_{0.5}\text{O}_{5+\delta}$  (PBSCF) and 3D porous N-doped graphene, which possessed an excellent ORR/OER catalytic activity and stability that could be attributed to the synergistic effect between PBSCF and N-doped graphene.<sup>[214]</sup> Recent studies have suggested that carbon components in the carbon-perovskite composites played multiple roles for the improved ORR/OER activity, such as improving the electrical conductivity, tuning the electronic structure of B-site metal, changing the crystal structure.<sup>[35,155,220]</sup>

#### 4.3. Carbon-Other Metal Compound Composites

Besides metal oxides, other transition metal compounds have also been investigated as bifunctional oxygen electrocatalysts, including metal hydroxides,<sup>[221–226]</sup> phosphides,<sup>[227–231]</sup> carbides,<sup>[232–235]</sup> chalcogenides,<sup>[236–247]</sup> nitrides,<sup>[248–250]</sup> etc. The electronic structures of the metal cations can be modified through the rational regulation of the adjacent anions to optimize the electrocatalytic activity.

Zhang et al. prepared a FeCo-DHO/NCNTs material that was composed of Fe/Co double hydroxide (FeCo-DHO) nanoparticles on multi-walled and N-doped CNTs (NCNTs) as high-performance bifunctional ORR/OER electrocatalyst (Figure 22a).<sup>[251]</sup> The strong interactions between FeCo-DHO and NCNTs not only facilitates the fast electron transfer and mass transport but also contributes to the enhanced corrosion resistance and high chemical stability, resulting in superior bifunctional ORR/OER activity and stability of the FeCo-DHO/NCNTs ( $\Delta E=0.96$  V, Figure 22b). Metal hydroxides can be further modified by anion modulation to achieve better intrinsic reactivity and electrical conductivity. In a recent work, Co-based hydroxides were converted into hydroxysulfides with good morphology preservation by simply immersing the hydroxide precursor into a solution with high  $\text{S}^{2-}$  concentration at room temperature.<sup>[252]</sup> TEM image of the as-prepared  $\text{Co}_3\text{FeS}_{1.5}(\text{OH})_6$  nanoparticles supported on N-doped graphene is presented in Figure 22c. S atoms can alter the Co oxidation state and facilitate the interaction between Co and oxygen-

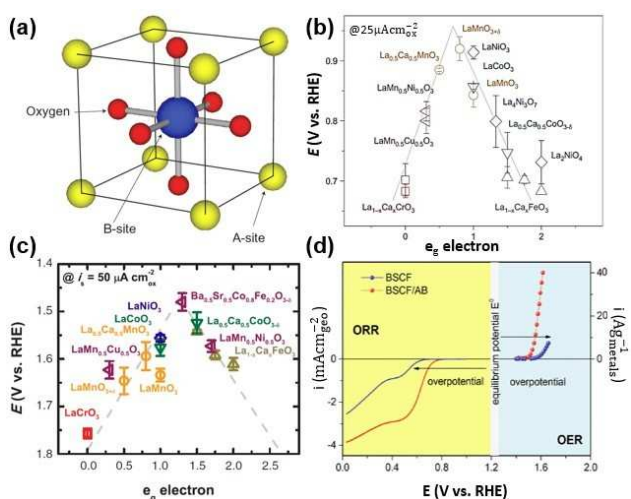


**Figure 21.** a) Typical perovskite crystal structure. b) Potentials at  $25 \text{ mA cm}^{-2}_{\text{ox}}$  as a function of  $e_g$  orbital in perovskite-based oxides. Reproduced with permission.<sup>[10]</sup> Copyright 2011, Springer Nature. c) Potentials at  $50 \text{ } \mu\text{A cm}^{-2}_{\text{ox}}$  of OER current as a function of  $e_g$  orbital in some perovskite-based oxides. Reproduced with permission.<sup>[202]</sup> Copyright 2011, American Association for the Advancement of Science. d) ORR and OER currents for BSCF single material electrode and BSCF/AB composite electrode in  $\text{O}_2$ -saturated 0.1 M KOH electrolyte. Reproduced with permission.<sup>[203]</sup> Copyright 2015, Wiley-VCH.

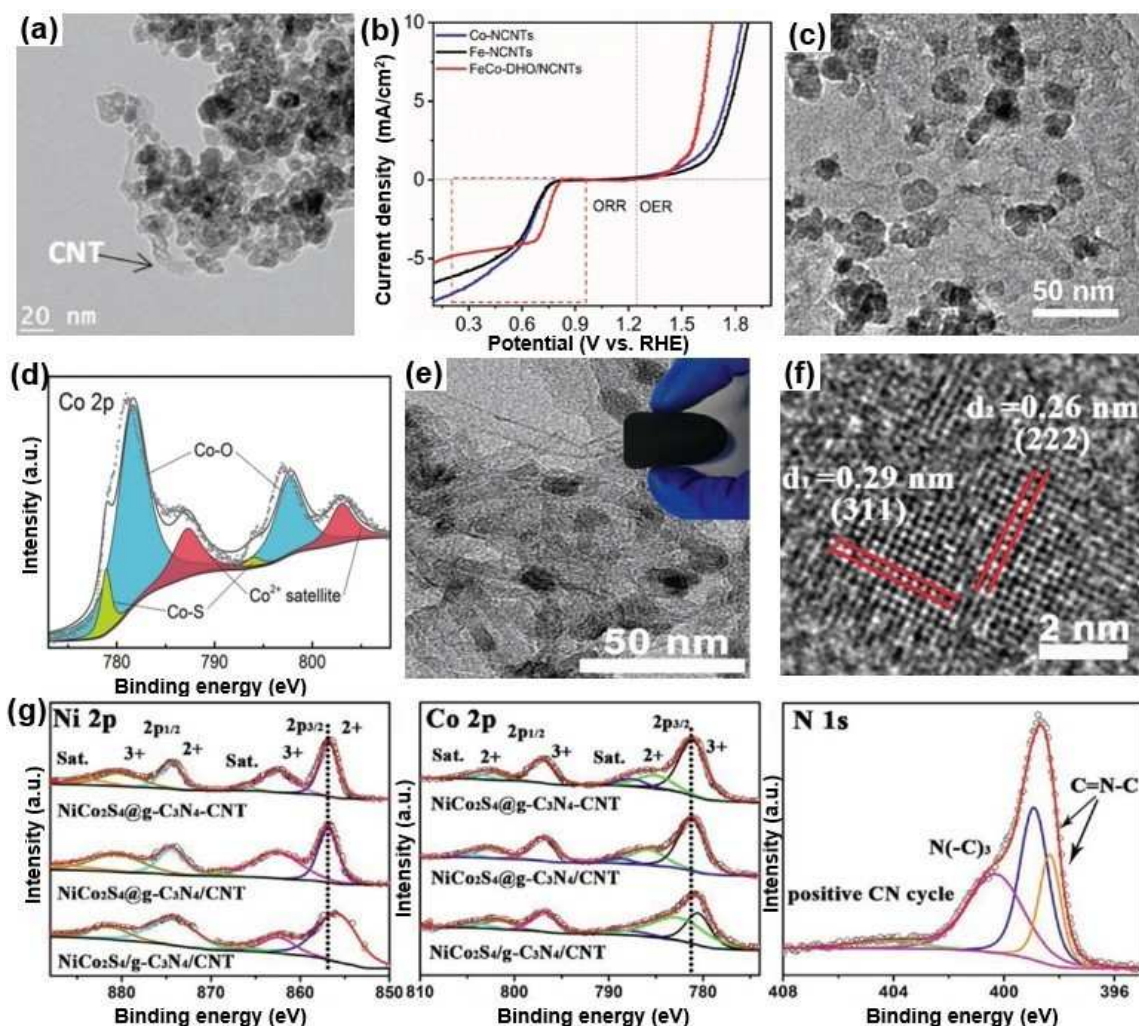


**Figure 22.** a) TEM image of FeCo-DHO/NCNTs. b) LSV of OER and ORR in O<sub>2</sub>-saturated 0.1 M KOH (scan rate 5 mV s<sup>-1</sup>). Reproduced with permission.<sup>[251]</sup> Copyright 2018, Wiley-VCH. c) TEM image of Co<sub>3</sub>FeS<sub>1.5</sub>(OH)<sub>6</sub> dispersed on 3D N-doped graphene framework. d) XPS Co 2p spectrum of Co<sub>3</sub>FeS<sub>1.5</sub>(OH)<sub>6</sub>. Reproduced with permission.<sup>[252]</sup> Copyright 2017, Wiley-VCH. e) TEM image of NiCo<sub>2</sub>S<sub>4</sub>@g-C<sub>3</sub>N<sub>4</sub>-CNT with the inset showing a photograph of NiCo<sub>2</sub>S<sub>4</sub>@g-C<sub>3</sub>N<sub>4</sub>-CNT hybrid film. f) HRTEM image showing the lattice fringes corresponding to the (222) and (311) planes of NiCo<sub>2</sub>S<sub>4</sub>. g) Ni 2p, Co 2p, and N 1s XPS spectra of investigated catalysts. Reproduced with permission.<sup>[253]</sup> Copyright 2019, Wiley-VCH.

containing intermediates in the oxygen electrocatalytic process by forming Co–S bonds (Figure 22d), leading to enhanced intrinsic activity. The catalyst exhibited excellent ORR ( $E_{1/2} = 0.72$  V) and OER ( $E_{10} = 1.59$  V) catalytic activity, with the small  $\Delta E$  of 0.87 V, enabling a high performance for rechargeable ZABs with a low overpotential of 0.86 V at 20 mA cm<sup>-2</sup>, a high specific capacity of 898 mAh g<sup>-1</sup>, and a long cycling life. Han et al. reported a novel NiCo<sub>2</sub>S<sub>4</sub>@g-C<sub>3</sub>N<sub>4</sub>-CNT hybrid electrocatalyst composed of NiCo<sub>2</sub>S<sub>4</sub> nanoparticles in situ grown on g-C<sub>3</sub>N<sub>4</sub> nanosheets (NiCo<sub>2</sub>S<sub>4</sub>@g-C<sub>3</sub>N<sub>4</sub>) and conductive CNTs, which wrap on the surface of NiCo<sub>2</sub>S<sub>4</sub>@g-C<sub>3</sub>N<sub>4</sub> to form a 3D porous architecture (Figure 22 e, f).<sup>[253]</sup> XPS analysis (Figure 22g) revealed a peak shift of Ni 2p<sub>3/2</sub> and Co 2p<sub>3/2</sub> to higher binding energies and split peak at 397.5 eV, indicating the electron transfer from Ni and Co sites to the abundant pyridinic-N in the underlying g-C<sub>3</sub>N<sub>4</sub> and the covalent coupling between g-C<sub>3</sub>N<sub>4</sub> and CNT for enhanced bifunctional activity. DFT calculations suggested a dual-site mechanism, namely, coactivation of Ni,

Co by forming a Ni, Co-N<sub>2</sub> moiety center, which simultaneously downshifts the d-band center position and weakens the bonding strength with oxygen intermediates, accelerating the reaction kinetics. As a result, the NiCo<sub>2</sub>S<sub>4</sub>@g-C<sub>3</sub>N<sub>4</sub>-CNT hybrid catalyst manifested remarkable bifunctional activity ( $\Delta E = 0.8$  V) and stability, enabling excellent discharge/charge performance of ZABs.

To provide the readers a more vivid illustration of the recent advances in this field, the ORR and OER performances of representative recently reported works are summarized in Table 1. We hope this can provide an overview of the superior bifunctional oxygen catalytic activity of carbon-based nanomaterials.

**Table 1.** ORR/OER bifunctional activity of selected carbon-based electrocatalysts in 0.1 M KOH.

Catalyst	Active material	$E_{1/2}$ or $E_{-3/2}$ /V	$E_{10}/V$	$\Delta E/V$	Ref
CNT@NCNT	N-doped carbon layer	0.70	1.75	1.05	<i>Adv. Funct. Mater.</i> <b>2014</b> , <i>24</i> , 5956.
NGSH N-PC@G	N-doped graphene/SWNT	0.68	1.63	0.95	<i>Small</i> <b>2014</b> , <i>10</i> , 2251
	N-doped porous carbon@graphene	0.8	1.63	0.83	<i>Carbon</i> <b>2016</b> , <i>106</i> , 74
NCMT-1000 (3D)	N-doped carbon microtube	0.71	1.52	0.81	<i>Energ. Environ. Sci.</i> <b>2016</b> , <i>9</i> , 3079
NCNF-1000	N-doped nanoporous carbon nanofiber films	0.82	1.84	1.02	<i>Adv. Mater.</i> <b>2016</b> , <i>28</i> , 3000
3D NCNT array	3D N-doped CNT array	0.81	1.65	0.84	<i>Nano Energy</i> <b>2017</b> , <i>37</i> , 98
NCNTFs	N doped CNT frameworks	0.87	1.60	0.73	<i>Nat. Energy</i> <b>2016</b> , <i>1</i> , 15006
2D-PPCN	P-doped carbon	0.85	1.59	0.74	<i>ACS Catal.</i> <b>2018</b> , <i>8</i> , 2464
N, P-GCNS	N and P co-doped graphene/carbon nanosheets	0.85	1.57	0.72	<i>ACS Catal.</i> <b>2015</b> , <i>5</i> , 4133
PCN-CFP	P-doped g-C <sub>3</sub> N <sub>4</sub> grown on carbon-fiber paper	0.67	1.53	0.96	<i>Angew. Chem. Int. Ed.</i> <b>2015</b> , <i>54</i> , 4646
SWCNT@NPC	Porous N, P co-doped carbon	0.85	1.68	0.83	<i>Carbon</i> <b>2018</b> , <i>139</i> , 156
PNGF	P, N co-doped graphene	0.85	1.55	0.70	<i>Energ. Environ. Sci.</i> <b>2017</b> , <i>10</i> , 1186
NPBC	N, P co-doped carbon	0.86	1.68	0.82	<i>Electrochim. Acta</i> <b>2017</b> , <i>257</i> , 250
P, S-CNS	P, S co-doped carbon nitride	0.87	1.56	0.69	<i>ACS Nano</i> <b>2017</b> , <i>11</i> , 347
DN-CP@G	Defect-enriched and pyridinic-N dominated carbon	0.80	1.79	0.99	<i>Adv. Energy Mater.</i> <b>2018</b> , <i>8</i> , 1703539
SHG	N, S co-doped graphitic sheets	0.87	1.56	0.78	<i>Adv. Mater.</i> <b>2017</b> , <i>29</i> , 1604942
NHC	N-doped defective carbon	0.88	1.68	0.80	<i>Nano Res.</i> <b>2017</b> , <i>10</i> , 1163
o-CC-H <sub>2</sub>	Defective graphene on carbon fiber	0.61	1.62	1.01	<i>Energy Storage Mater.</i> <b>2018</b> , <i>15</i> , 124
2D-PPCN	P-doped porous carbon nanosheets	0.85	1.60	0.75	<i>ACS Catal.</i> <b>2018</b> , <i>8</i> , 2464
O-NGM-800	N-doped nanocarbon with abundant O-induced vacancies	0.86	1.70	0.84	<i>Adv. Mater.</i> <b>2019</b> , <i>31</i> , 1803339
MSZIF-900	Co supported on N-doped CNT	0.84	1.57	0.73	<i>Angew. Chem. Int. Ed.</i> <b>2017</b> , <i>56</i> , 13781
Co/N-CNTs	Co nanoparticles (NPs) encapsulated in N-doped CNTs	0.84	1.62	0.78	<i>J. Mater. Chem. A</i> <b>2016</b> , <i>4</i> , 1694
FeN <sub>x</sub> -PNC	Fe–N <sub>x</sub> species in carbon	0.86	1.63	0.77	<i>ACS Nano</i> <b>2018</b> , <i>12</i> , 1949
Meso-CoNC@GF	mesoporous CoNC NPs coated graphene framework	0.87	1.67	0.80	<i>Adv. Mater.</i> <b>2018</b> , <i>30</i> , 1704898
NC–Co SA	Co single atoms on N-doped porous carbon nanoflake arrays	0.87	1.59	0.72	<i>ACS Catal.</i> <b>2018</b> , <i>8</i> , 8961
Co–N <sub>x</sub> /C NRA	Co–N <sub>x</sub> doped carbon	0.88	1.53	0.65	<i>Adv. Funct. Mater.</i> <b>2018</b> , <i>28</i> , 1704638
S, N–Fe/N/C–CNT	Atomically dispersed Fe–N <sub>x</sub> on N, S co-doped carbon layers	0.85	1.60	0.75	<i>Angew. Chem. Int. Ed.</i> <b>2017</b> , <i>56</i> , 610
NC@Co–NGC	Double-shelled nanocages composed of N-doped microporous carbon and Co-decorated N-doped mesoporous carbon	0.82	1.64	0.82	<i>Adv. Mater.</i> <b>2017</b> , <i>29</i> , 1700874
CNCN-44	Co–N embedded in CNTs	0.79	1.61	0.82	<i>J. Mater. Chem. A</i> <b>2016</b> , <i>4</i> , 4864
meso/micro-FeCo-N <sub>x</sub> -30	2D meso/microporous Fe/Co–N <sub>x</sub> -doped carbon nanosheets	0.89	1.67	0.78	<i>Angew. Chem. Int. Ed.</i> <b>2018</b> , <i>57</i> , 1856.
Co–Fe/N–GCT	CoFe NPs embedded in N-doped bamboo-like CNTs tangled with rGO nanosheets	0.79	1.67	0.88	<i>Angew. Chem. Int. Ed.</i> <b>2018</b> , <i>57</i> , 16166
NiCo/PFC	NiCo NPs anchored on porous fibrous carbon aerogels	0.77	1.63	0.86	<i>Nano Lett.</i> <b>2016</b> , <i>16</i> , 6516

**Table 1.** continued

Catalyst	Active material	$E_{1/2}$ or $E_{-3}/V$	$E_{10}/V$	$\Delta E/V$	Ref
N-GCNT/FeCo	FeCo NPs encapsulated in in situ grown N-doped graphitic CNTs with bamboo-like structure	0.92	1.73	0.81	<i>Adv. Energy Mater.</i> 2017, 7, 1602420
Co@Co <sub>3</sub> O <sub>4</sub> /NC-1	core-shell Co@Co <sub>3</sub> O <sub>4</sub> NPs embedded in CNT-grafted N-doped carbon-polyhedra	0.80	1.65	0.85	<i>Angew. Chem. Int. Ed.</i> 2016, 55, 4087
Co-NC@Al <sub>2</sub> O <sub>3</sub>	Co <sub>3</sub> O <sub>4</sub> -embedded N-doped porous carbon	0.86	1.65	0.79	<i>Adv. Mater.</i> 2018, 30, 1805268
CoZn-NC-700	CoO–Co wrapped with N-doped carbon	0.84	1.62	0.78	<i>Adv. Funct. Mater.</i> 2017, 27, 1700795
NC-Co <sub>3</sub> O <sub>4</sub> -90/CC	Hollow Co <sub>3</sub> O <sub>4</sub> nanospheres embedded within N-doped carbon nanowall arrays	0.87	1.59	0.72	<i>Adv. Mater.</i> 2017, 29, 1704117
Ni-MnO/rGO	3D porous graphene aerogel-supported Ni/MnO NPs	0.78	1.60	0.82	<i>Adv. Mater.</i> 2018, 30, 1704609
Co <sub>3</sub> O <sub>4</sub> /N-rGo	Atomically thin mesoporous Co <sub>3</sub> O <sub>4</sub> layers strongly coupled with N-rGO nano-sheets	0.79	1.72	0.93	<i>Adv. Mater.</i> 2018, 30, 1703657
Ni <sub>3</sub> Fe/N-C	Ni <sub>3</sub> Fe NPs embedded in N-doped 2D porous graphitic carbon sheets	0.78	1.62	0.84	<i>Adv. Energy Mater.</i> 2017, 7, 1601172
Ni <sub>3</sub> FeN/Co, N-CNF	Ni <sub>3</sub> FeN in Co, N co-doped carbon nanoframe	0.81	1.50	0.69	<i>Carbon</i> 2018, 130, 112
Fe <sub>0.5</sub> Ni <sub>0.5</sub> @N-GR	NiFe NPs wrapped with N-doped graphite	0.83	1.44	0.61	<i>Adv. Funct. Mater.</i> 2018, 28, 1706928
CoO <sub>0.87</sub> S <sub>0.13</sub> /GN	Cobalt oxysulfide on N-doped graphene	0.83	1.59	0.76	<i>Adv. Mater.</i> 2017, 29, 1702526
NiCo <sub>2</sub> S <sub>4</sub> /N-CNT	NiCo <sub>2</sub> S <sub>4</sub> NCs anchored on N-doped CNT	0.80	1.60	0.80	<i>Nano Energy</i> 2017, 31, 541
CoP-DC	Defective carbon-CoP hybrids	0.81	1.55	0.74	<i>Adv. Energy Mater.</i> 2018, 8, 1703623
NiFe-LDH/Co, N-CNF	NiFe hydroxide on Co, N co-doped carbon	0.79	1.54	0.75	<i>Adv. Energy Mater.</i> 2017, 7, 1700467.
Co <sub>3</sub> FeS <sub>1.5</sub> (OH) <sub>6</sub>	Co <sub>3</sub> FeS <sub>1.5</sub> (OH) <sub>6</sub> supported on 3D N-doped graphene framework	0.72	1.59	0.87	<i>Adv. Mater.</i> 2017, 29, 1702327

## 5. Summary and Outlook

The recent advances of carbon-based nanomaterials as efficient bifunctional oxygen catalysts for ZABs have been summarized (Figure 23). Nanostructured carbon provides a flexible platform

to rationally regulate the electronic structure of the active sites to achieve high bifunctional activity through multiple strategies. The state-of-the-art bifunctional oxygen electrocatalysts can deliver a  $\Delta E$  approaching 0.65 V, enabling promising applications in rechargeable ZABs. Despite the intensive research and great improvements achieved, there are still challenges remaining, as presented in the following:

- 1) The catalytic performance of a bifunctional oxygen electrocatalyst is affected by various factors, e.g., the intrinsic activity, the electrical conductivity, the number of accessible active sites, testing conditions and methods. Therefore, standards for evaluating the materials' performance should be established to identify the main factors governing the catalyst activity as well as to gain deeper understanding of the intrinsic performance of novel electrocatalysts. This should provide guidelines for the rational design of efficient oxygen electrocatalysts via proper regulation strategies.
- 2) Further efforts are also required to monitor the complex reaction processes of oxygen catalysis to gain in-depth understandings of the reaction mechanisms. Advanced in situ characterization techniques can provide real-time insights into the evolution of critical intermediates and by-products, facilitating to disclose key information in respects of reaction pathway, surface/interface behaviour, and performance degradation. In combination with theoretical modelling, this can help to uncover the reactivity of oxygen



**Figure 23.** Schematic illustration of designing carbon-based nanomaterials as efficient bifunctional oxygen catalysts.

- catalysts at the atomic level, guiding the rational design of high-performance electrocatalysts.
- 3) Currently the catalyst studies are mainly based on the three-electrode setup and the rotating disk electrode (RDE) technique, which may not always properly reflect the practical working environments in real ZABs. Catalysts that show high activity in the lab may not perform well in commercially relevant ZAB devices, especially under high current densities and operating temperatures. Therefore, catalysts are encouraged to be tested under practical conditions to establish a comparable link between lab results and commercial applications.
- 4) Last but not the least, the overall performance of a ZAB is also strongly affected by other components (e.g., Zn anode, separator, electrolyte) as well as cell configuration. Future research efforts are also required to cover relevant issues like structural modification of Zn anode to alleviate dendrite growth and corrosion, novel electrolyte technologies to address leakage of electrolyte, optimization of separators with improved selectivity, etc. The synergistic enhancement should largely benefit the scale-up production and commercialization of zinc-air batteries.

Overall, ZABs are one of the most promising electrochemical energy conversion and storage systems with the high energy density and other intrinsic advantages. The development of highly efficient bifunctional oxygen catalysts is of great significance and remains a challenging topic. This review aims to offer a timely progress report on the recent research progress of carbon-based bifunctional oxygen electrocatalysts and their applications in ZABs. Moreover, we hope this review can provide some useful insights for the future research in this field. The rapid growth of low-cost, highly efficient bifunctional ORR/OER electrocatalysts, together with advances in air-electrode design, should largely accelerate the development and commercialization of ZABs in the future.

## Acknowledgements

This work is supported by the China Scholarship Council (No. 201804910018), the National Natural Science Foundation of China (No. 51502045), and the Australian Research Council under the Discovery Early Career Researcher Award (DECRA, No. DE170100871).

## Conflict of Interest

The authors declare no conflict of interest.

**Keywords:** zinc-air batteries • carbon nanomaterials • oxygen reduction reaction • oxygen evolution reaction • electrocatalysis

[1] V. Etacheri, R. Marom, R. Elazari, G. Salitra, D. Aurbach, *Energy Environ. Sci.* 2011, 4, 3243–3262.

- [2] F. Wang, X. Wu, C. Li, Y. Zhu, L. Fu, Y. Wu, X. Liu, *Energy Environ. Sci.* 2016, 9, 3570–3611.
- [3] Z. Wu, Y. Wang, X. Liu, C. Lv, Y. Li, D. Wei, Z. Liu, *Adv. Mater.* 2019, 31, 1800716.
- [4] P. Lu, X. Wang, L. Wen, X. Jiang, W. Guo, L. Wang, X. Yan, F. Hou, J. Liang, H.-M. Cheng, S. X. Dou, *Small* 2019, 15, 1805064.
- [5] L. Wang, Z. Zhou, X. Yan, F. Hou, L. Wen, W. Luo, J. Liang, S. X. Dou, *Energy Storage Mater.* 2018, 14, 22–48.
- [6] H. Yuan, J.-Q. Huang, H.-J. Peng, M.-M. Titirici, R. Xiang, R. Chen, Q. Liu, Q. Zhang, *Adv. Energy Mater.* 2018, 8, 1802107.
- [7] Q. Zhang, F. Li, J.-Q. Huang, H. Li, *Adv. Funct. Mater.* 2018, 28, 1804589.
- [8] X. Hong, J. Mei, L. Wen, Y. Tong, A. J. Vasileff, L. Wang, J. Liang, Z. Sun, S. X. Dou, *Adv. Mater.* 2019, 31, 1802822.
- [9] H.-J. Peng, J.-Q. Huang, Q. Zhang, *Chem. Soc. Rev.* 2017, 46, 5237–5288.
- [10] J. Suntivich, H. A. Gasteiger, N. Yabuuchi, H. Nakanishi, J. B. Goodenough, Y. Shao-Horn, *Nat. Chem.* 2011, 3, 546.
- [11] Y. Zheng, D.-S. Yang, J. M. Kweun, C. Li, K. Tan, F. Kong, C. Liang, Y. J. Chabal, Y. Y. Kim, M. Cho, J.-S. Yu, K. Cho, *Nano Energy* 2016, 30, 443–449.
- [12] Y. Li, H. Dai, *Chem. Soc. Rev.* 2014, 43, 5257–5275.
- [13] J. Fu, Z. P. Cano, M. G. Park, A. Yu, M. Fowler, Z. Chen, *Adv. Mater.* 2017, 29, 1604685.
- [14] P. Tan, B. Chen, H. Xu, H. Zhang, W. Cai, M. Ni, M. Liu, Z. Shao, *Energy Environ. Sci.* 2017, 10, 2056–2080.
- [15] X. Chen, Z. Zhou, H. E. Karahan, Q. Shao, L. Wei, Y. Chen, *Small* 2018, 14, 1801929.
- [16] J. Fu, R. Liang, G. Liu, A. Yu, Z. Bai, L. Yang, Z. Chen, *Adv. Mater.* 2019, DOI: 10.1002/adma.201805230.
- [17] X. Han, X. Li, J. White, C. Zhong, Y. Deng, W. Hu, T. Ma, *Adv. Energy Mater.* 2018, 8, 1801396.
- [18] H.-F. Wang, C. Tang, Q. Zhang, *Adv. Funct. Mater.* 2018, 28, 1803329.
- [19] J.-S. Lee, T. S. Kim, R. Cao, N.-S. Choi, M. Liu, K. T. Lee, J. Cho, *Adv. Energy Mater.* 2011, 1, 34–50.
- [20] H. Kim, G. Jeong, Y.-U. Kim, J.-H. Kim, C.-M. Park, H.-J. Sohn, *Chem. Soc. Rev.* 2013, 42, 9011–9034.
- [21] Z. P. Cano, D. Banham, S. Ye, A. Hintennach, J. Lu, M. Fowler, Z. Chen, *Nat. Energy* 2018, 3, 279–289.
- [22] Y. Zheng, Y. Jiao, S. Z. Qiao, *Adv. Mater.* 2015, 27, 5372–5378.
- [23] L. Ji, P. Meduri, V. Agubra, X. Xiao, M. Alcoutlabi, *Adv. Energy Mater.* 2016, 6, 1502159.
- [24] M. Kuang, G. Zheng, *Small* 2016, 12, 5656–5675.
- [25] T. Y. Ma, S. Dai, S. Z. Qiao, *Mater. Today* 2016, 19, 265–273.
- [26] H. Cui, Z. Zhou, D. Jia, *Mater. Horiz.* 2017, 4, 7–19.
- [27] C. Tang, Q. Zhang, *Adv. Mater.* 2017, 29, 1604103.
- [28] D. Yang, L. Zhang, X. Yan, X. Yao, *Small Methods* 2017, 1, 1700209.
- [29] Y. P. Zhu, C. Guo, Y. Zheng, S. Z. Qiao, *Acc. Chem. Res.* 2017, 50, 915–923.
- [30] C. Tang, H.-F. Wang, Q. Zhang, *Acc. Chem. Res.* 2018, 51, 881–889.
- [31] H.-F. Wang, R. Chen, J. Feng, M. Qiao, S. Doszczeczko, Q. Zhang, A. B. Jorge, M.-M. Titirici, *ChemElectroChem* 2018, 5, 1786–1804.
- [32] S. Wang, Z. Teng, C. Wang, G. Wang, *ChemSusChem* 2018, 11, 2267–2295.
- [33] W. Li, R. Fang, Y. Xia, W. Zhang, X. Wang, X. Xia, J. Tu, *Batteries & Supercaps* 2019, 2, 9–36.
- [34] D. Song, W. Guo, T. Zhang, P. Lu, A. Guo, F. Hou, X. Yan, J. Liang, *Surf. Innovations* 2019, 7, 10–17.
- [35] E. Davari, D. G. Ivey, *Sustain. Energ. Fuels* 2018, 2, 39–67.
- [36] F. Calle-Vallejo, J. I. Martínez, J. Rossmeisl, *Phys. Chem. Chem. Phys.* 2011, 13, 15639–15643.
- [37] J. Rossmeisl, Z. W. Qu, H. Zhu, G. J. Kroes, J. K. Nørskov, *J. Electroanal. Chem.* 2007, 607, 83–89.
- [38] A. Vojodic, J. K. Nørskov, *Natl. Sci. Rev.* 2015, 2, 140–143.
- [39] I. C. Man, H.-Y. Su, F. Calle-Vallejo, H. A. Hansen, J. I. Martínez, N. G. Inoglu, J. Kitchin, T. F. Jaramillo, J. K. Nørskov, J. Rossmeisl, *ChemCatChem* 2011, 3, 1159–1165.
- [40] Z. W. Seh, J. Kibsgaard, C. F. Dickens, I. Chorkendorff, J. K. Nørskov, T. F. Jaramillo, *Science* 2017, 355, eaad4998.
- [41] Y. Jiao, Y. Zheng, M. Jaroniec, S. Z. Qiao, *J. Am. Chem. Soc.* 2014, 136, 4394–4403.
- [42] J. K. Nørskov, T. Bligaard, J. Rossmeisl, C. H. Christensen, *Nat. Chem.* 2009, 1, 37.
- [43] Y. Gorlin, T. F. Jaramillo, *J. Am. Chem. Soc.* 2010, 132, 13612–13614.
- [44] G.-L. Tian, Q. Zhang, B. Zhang, Y.-G. Jin, J.-Q. Huang, D. S. Su, F. Wei, *Adv. Funct. Mater.* 2014, 24, 5956–5961.

- [45] G.-L. Tian, M.-Q. Zhao, D. Yu, X.-Y. Kong, J.-Q. Huang, Q. Zhang, F. Wei, *Small* **2014**, *10*, 2251–2259.
- [46] J.-C. Li, P.-X. Hou, S.-Y. Zhao, C. Liu, D.-M. Tang, M. Cheng, F. Zhang, H.-M. Cheng, *Energy Environ. Sci.* **2016**, *9*, 3079–3084.
- [47] S. Patra, R. Choudhary, E. Roy, R. Madhuri, P. K. Sharma, *Nano Energy* **2016**, *30*, 118–129.
- [48] H. B. Yang, J. Miao, S.-F. Hung, J. Chen, H. B. Tao, X. Wang, L. Zhang, R. Chen, J. Gao, H. M. Chen, L. Dai, B. Liu, *Sci. Adv.* **2016**, *2*, e1501122.
- [49] S. Liu, H. Zhang, Q. Zhao, X. Zhang, R. Liu, X. Ge, G. Wang, H. Zhao, W. Cai, *Carbon* **2016**, *106*, 74–83.
- [50] A. M. El-Sawy, I. M. Mosa, D. Su, C. J. Guild, S. Khalid, R. Joesten, J. F. Rusling, S. L. Suib, *Adv. Energy Mater.* **2016**, *6*, 1501966.
- [51] K. Qu, Y. Zheng, S. Dai, S. Z. Qiao, *Nano Energy* **2016**, *19*, 373–381.
- [52] W. Xia, A. Mahmood, Z. Liang, R. Zou, S. Guo, *Angew. Chem. Int. Ed.* **2016**, *55*, 2650–2676; *Angew. Chem.* **2016**, *128*, 2698–2726.
- [53] W. Lei, Y.-P. Deng, G. Li, Z. P. Cano, X. Wang, D. Luo, Y. Liu, D. Wang, Z. Chen, *ACS Catal.* **2018**, *8*, 2464–2472.
- [54] X. Cai, L. Lai, J. Lin, Z. Shen, *Mater. Horiz.* **2017**, *4*, 945–976.
- [55] B. Fang, J. Yang, C. Chen, C. Zhang, D. Chang, H. Xu, C. Gao, *ChemCatChem* **2017**, *9*, 4520–4528.
- [56] J. Zhang, Z. Zhao, Z. Xia, L. Dai, *Nat. Nanotechnol.* **2015**, *10*, 444.
- [57] R. Li, Z. Wei, X. Gou, *ACS Catal.* **2015**, *5*, 4133–4142.
- [58] P. Li, H. Jang, J. Zhang, M. Tian, S. Chen, B. Yuan, Z. Wu, X. Liu, J. Cho, *ChemElectroChem* **2019**, *6*, 393–397.
- [59] H. Li, W. Wan, X. Liu, H. Liu, S. Shen, F. Lv, J. Luo, *ChemElectroChem* **2018**, *5*, 1113–1119.
- [60] L. Zhou, C. Zhang, X. Cai, Y. Qian, H. Jiang, B. Li, L. Lai, Z. Shen, W. Huang, *ChemElectroChem* **2018**, *5*, 1811–1816.
- [61] Q. Wang, Y. Li, K. Wang, J. Zhou, L. Zhu, L. Gu, J. Hu, X. Cao, *Electrochim. Acta* **2017**, *257*, 250–258.
- [62] Y. Zheng, Y. Jiao, M. Jaroniec, Y. Jin, S. Z. Qiao, *Small* **2012**, *8*, 3550–3566.
- [63] J.-T. Ren, G.-G. Yuan, C.-C. Weng, L. Chen, Z.-Y. Yuan, *ChemCatChem* **2018**, *10*, 5297–5305.
- [64] T. Y. Ma, J. Ran, S. Dai, M. Jaroniec, S. Z. Qiao, *Angew. Chem. Int. Ed.* **2015**, *54*, 4646–4650; *Angew. Chem.* **2015**, *127*, 4729–4733.
- [65] G.-L. Chai, K. Qiu, M. Qiao, M.-M. Titirici, C. Shang, Z. Guo, *Energy Environ. Sci.* **2017**, *10*, 1186–1195.
- [66] J.-C. Li, P.-X. Hou, M. Cheng, C. Liu, H.-M. Cheng, M. Shao, *Carbon* **2018**, *139*, 156–163.
- [67] Z. Zhao, Z. Yuan, Z. Fang, J. Jian, J. Li, M. Yang, C. Mo, Y. Zhang, X. Hu, P. Li, S. Wang, W. Hong, Z. Zheng, G. Ouyang, X. Chen, D. Yu, *Adv. Sci.* **2018**, *5*, 1800760.
- [68] C. Hu, L. Dai, *Adv. Mater.* **2017**, *29*, 1604942.
- [69] H. Fan, Y. Wang, F. Gao, L. Yang, M. Liu, X. Du, P. Wang, L. Yang, Q. Wu, X. Wang, Z. Hu, *J. Energy Chem.* **2019**, *34*, 64–71.
- [70] Y. Qian, Z. Hu, X. Ge, S. Yang, Y. Peng, Z. Kang, Z. Liu, J. Y. Lee, D. Zhao, *Carbon* **2017**, *111*, 641–650.
- [71] S. S. Shinde, C.-H. Lee, A. Sami, D.-H. Kim, S.-U. Lee, J.-H. Lee, *ACS Nano* **2017**, *11*, 347–357.
- [72] S. S. Shinde, J.-Y. Yu, J.-W. Song, Y.-H. Nam, D.-H. Kim, J.-H. Lee, *Nanoscale Horiz.* **2017**, *2*, 333–341.
- [73] Q. Liu, Y. Wang, L. Dai, J. Yao, *Adv. Mater.* **2016**, *28*, 3000–3006.
- [74] M. Yang, X. Hu, Z. Fang, L. Sun, Z. Yuan, S. Wang, W. Hong, X. Chen, D. Yu, *Adv. Funct. Mater.* **2017**, *27*, 1701971.
- [75] W. Luo, B. Wang, C. G. Heron, M. J. Allen, J. Morre, C. S. Maier, W. F. Stickle, X. Ji, *Nano Lett.* **2014**, *14*, 2225–2229.
- [76] X. Lu, W.-L. Yim, B. H. R. Suryanto, C. Zhao, *J. Am. Chem. Soc.* **2015**, *137*, 2901–2907.
- [77] Z. Pei, H. Li, Y. Huang, Q. Xue, Y. Huang, M. Zhu, Z. Wang, C. Zhi, *Energy Environ. Sci.* **2017**, *10*, 742–749.
- [78] J.-T. Ren, Z.-Y. Yuan, *ChemCatChem* **2018**, *10*, 3260–3268.
- [79] H. Wu, J. Geng, H. Ge, Z. Guo, Y. Wang, G. Zheng, *Adv. Energy Mater.* **2016**, *6*, 1600794.
- [80] L. Wang, Y. Wang, M. Wu, Z. Wei, C. Cui, M. Mao, J. Zhang, X. Han, Q. Liu, J. Ma, *Small* **2018**, *14*, 1800737.
- [81] T. Y. Ma, S. Dai, M. Jaroniec, S. Z. Qiao, *Angew. Chem. Int. Ed.* **2014**, *53*, 7281–7285; *Angew. Chem.* **2014**, *126*, 7409–7413.
- [82] M. Wu, Y. Wang, Z. Wei, L. Wang, M. Zhuo, J. Zhang, X. Han, J. Ma, *J. Mater. Chem. A* **2018**, *6*, 10918–10925.
- [83] Y. Jia, L. Zhang, A. Du, G. Gao, J. Chen, X. Yan, C. L. Brown, X. Yao, *Adv. Mater.* **2016**, *28*, 9532–9538.
- [84] C. Tang, H.-F. Wang, X. Chen, B.-Q. Li, T.-Z. Hou, B. Zhang, Q. Zhang, M.-M. Titirici, F. Wei, *Adv. Mater.* **2016**, *28*, 6845–6851.
- [85] S. S. Shinde, C. H. Lee, J.-Y. Yu, D.-H. Kim, S. U. Lee, J.-H. Lee, *ACS Nano* **2018**, *12*, 596–608.
- [86] J. W. F. To, J. W. D. Ng, S. Siahrostami, A. L. Koh, Y. Lee, Z. Chen, K. D. Fong, S. Chen, J. He, W.-G. Bae, J. Wilcox, H. Y. Jeong, K. Kim, F. Studt, J. K. Nørskov, T. F. Jaramillo, Z. Bao, *Nano Res.* **2017**, *10*, 1163–1177.
- [87] Y. Jiang, L. Yang, T. Sun, J. Zhao, Z. Lyu, O. Zhao, X. Wang, Q. Wu, J. Ma, Z. Hu, *ACS Catal.* **2015**, *5*, 6707–6712.
- [88] Z. Lu, J. Wang, S. Huang, Y. Hou, Y. Li, Y. Zhao, S. Mu, J. Zhang, Y. Zhao, *Nano Energy* **2017**, *42*, 334–340.
- [89] T. Sun, J. Wang, C. Qiu, X. Ling, B. Tian, W. Chen, C. Su, *Adv. Sci.* **2018**, *5*, 1800036.
- [90] H.-F. Wang, C. Tang, B. Wang, B.-Q. Li, X. Cui, Q. Zhang, *Energy Storage Mater.* **2018**, *15*, 124–130.
- [91] J. Zhang, Y. Sun, J. Zhu, Z. Gao, S. Li, S. Mu, Y. Huang, *Adv. Sci.* **2018**, *5*, 1801375.
- [92] K. Kordek, L. Jiang, K. Fan, Z. Zhu, L. Xu, M. Al-Mamun, Y. Dou, S. Chen, P. Liu, H. Yin, P. Rutkowski, H. Zhao, *Adv. Energy Mater.* **2019**, *9*, 1802936.
- [93] M. Wang, W. Wang, T. Qian, S. Liu, Y. Li, Z. Hou, J. B. Goodenough, P. M. Ajayan, C. Yan, *Adv. Mater.* **2019**, *31*, 1803339.
- [94] D.-W. Wang, D. Su, *Energy Environ. Sci.* **2014**, *7*, 576–591.
- [95] J. Sun, S. E. Lowe, L. Zhang, Y. Wang, K. Pang, Y. Wang, Y. Zhong, P. Liu, K. Zhao, Z. Tang, H. Zhao, *Angew. Chem. Int. Ed.* **2018**, *57*, 16511–16515.
- [96] C. Hang, J. Zhang, J. Zhu, W. Li, Z. Kou, Y. Huang, *Adv. Energy Mater.* **2018**, *8*, 1703539.
- [97] X. Cai, B. Y. Xia, J. Franklin, B. Li, X. Wang, Z. Wang, L. Chen, J. Lin, L. Lai, Z. Shen, *J. Mater. Chem. A* **2017**, *5*, 2488–2495.
- [98] G. Fu, Z. Cui, Y. Chen, Y. Li, Y. Tang, J. B. Goodenough, *Adv. Energy Mater.* **2017**, *7*, 1601172.
- [99] J. Guo, T. Li, Q. Wang, N. Zhang, Y. Cheng, Z. Xiang, *Nanoscale* **2019**, *11*, 211–218.
- [100] Y. Fu, H.-Y. Yu, C. Jiang, T.-H. Zhang, R. Zhan, X. Li, J.-F. Li, J.-H. Tian, R. Yang, *Adv. Funct. Mater.* **2018**, *28*, 1705094.
- [101] B. Y. Guan, Y. Lu, Y. Wang, M. Wu, X. W. Lou, *Adv. Funct. Mater.* **2018**, *28*, 1706738.
- [102] Q. Qin, P. Li, L. Chen, X. Liu, *ACS Appl. Mater. Interfaces* **2018**, *10*, 39828–39838.
- [103] L. Yang, X. Zeng, D. Wang, D. Cao, *Energy Storage Mater.* **2018**, *12*, 277–283.
- [104] Z. Li, H. He, H. Cao, S. Sun, W. Diao, D. Gao, P. Lu, S. Zhang, Z. Guo, M. Li, R. Liu, D. Ren, C. Liu, Y. Zhang, Z. Yang, J. Jiang, G. Zhang, *Appl. Catal. B: Environ.* **2019**, *240*, 112–121.
- [105] H. Wu, M. Zeng, Z. Li, X. Zhu, C. Tian, C. Xia, L. He, S. Dai, *Sustain. Energ. Fuels* **2019**, *3*, 136–141.
- [106] N. Ma, Y. Jia, X. Yang, X. She, L. Zhang, Z. Peng, X. Yao, D. Yang, *J. Mater. Chem. A* **2016**, *4*, 6376–6384.
- [107] Z. Wang, Y. Lu, Y. Yan, T. Y. P. Larissa, X. Zhang, D. Wuu, H. Zhang, Y. Yang, X. Wang, *Nano Energy* **2016**, *30*, 368–378.
- [108] B. Y. Xia, Y. Yan, N. Li, H. B. Wu, X. W. Lou, X. Wang, *Nat. Energy* **2016**, *1*, 15006.
- [109] S. Liu, Z. Wang, S. Zhou, F. Yu, M. Yu, C.-Y. Chiang, W. Zhou, J. Zhao, J. Qiu, *Adv. Mater.* **2017**, *29*, 1700874.
- [110] M. Wang, T. Qian, J. Zhou, C. Yan, *ACS Appl. Mater. Interfaces* **2017**, *9*, 5213–5221.
- [111] Q.-L. Zhu, W. Xia, L.-R. Zheng, R. Zou, Z. Liu, Q. Xu, *ACS Energy Lett.* **2017**, *2*, 504–511.
- [112] M. Khalid, A. M. B. Honarato, H. Varela, L. Dai, *Nano Energy* **2018**, *45*, 127–135.
- [113] G. Zhong, S. Li, S. Xu, W. Liao, X. Fu, F. Peng, *ACS Sustainable Chem. Eng.* **2018**, *6*, 15108–15118.
- [114] Y. Qian, I. A. Khan, D. Zhao, *Small* **2017**, *13*, 1701143.
- [115] X. Zhang, J. Luo, H.-F. Lin, P. Tang, J. R. Morante, J. Arbiol, K. Wan, B.-W. Mao, L.-M. Liu, J. Fransaeer, *Energy Storage Mater.* **2019**, *17*, 46–61.
- [116] W. Zhang, X. Yao, S. Zhou, X. Li, L. Li, Z. Yu, L. Gu, *Small* **2018**, *14*, 1800423.
- [117] F. Meng, H. Zhong, D. Bao, J. Yan, X. Zhang, *J. Am. Chem. Soc.* **2016**, *138*, 10226–10231.
- [118] M. Kuang, Q. Wang, P. Han, G. Zheng, *Adv. Energy Mater.* **2017**, *7*, 1700193.
- [119] P. Liu, D. Gao, W. Xiao, L. Ma, K. Sun, P. Xi, D. Xue, J. Wang, *Adv. Funct. Mater.* **2018**, *28*, 1706928.
- [120] M. Shao, Q. Chang, J.-P. Dodelet, R. Chenitz, *Chem. Rev.* **2016**, *116*, 3594–3657.
- [121] J. Wang, F. Ciucci, *Small* **2017**, *13*, 1604103.

- [122] S. Wang, X. Yan, K.-H. Wu, X. Chen, J.-M. Feng, P. Lu, H. Feng, H.-M. Cheng, J. Liang, S. X. Dou, *Carbon* **2019**, *144*, 798–804.
- [123] W. Niu, K. Marcus, L. Zhou, Z. Li, L. Shi, K. Liang, Y. Yang, *ACS Catal.* **2018**, *8*, 1926–1931.
- [124] R. Nandan, A. Gautam, K. K. Nanda, *J. Mater. Chem. A* **2017**, *5*, 20252–20262.
- [125] S. Han, X. Hu, J. Wang, X. Fang, Y. Zhu, *Adv. Energy Mater.* **2018**, *8*, 1800955.
- [126] X. Liu, L. Wang, P. Yu, C. Tian, F. Sun, J. Ma, W. Li, H. Fu, *Angew. Chem. Int. Ed.* **2018**, *57*, 16166–16170.
- [127] G. Fu, Y. Chen, Z. Cui, Y. Li, W. Zhou, S. Xin, Y. Tang, J. B. Goodenough, *Nano Lett.* **2016**, *16*, 6516–6522.
- [128] G. Jia, W. Zhang, G. Fan, Z. Li, D. Fu, W. Hao, C. Yuan, Z. Zou, *Angew. Chem. Int. Ed.* **2017**, *56*, 13781–13785; *Angew. Chem.* **2017**, *129*, 13969–13973.
- [129] T. Wang, Z. Kou, S. Mu, J. Liu, D. He, I. S. Amiinu, W. Meng, K. Zhou, Z. Luo, S. Chaemchuen, F. Verpoort, *Adv. Funct. Mater.* **2018**, *28*, 1705048.
- [130] S. Liu, M. Wang, X. Sun, N. Xu, J. Liu, Y. Wang, T. Qian, C. Yan, *Adv. Mater.* **2018**, *30*, 1704898.
- [131] I. S. Amiinu, X. Liu, Z. Pu, W. Li, Q. Li, J. Zhang, H. Tang, H. Zhang, S. Mu, *Adv. Funct. Mater.* **2018**, *28*, 1704638.
- [132] Y. Zhang, H. Sun, Y. Qiu, X. Ji, T. Ma, F. Gao, Z. Ma, B. Zhang, P. Hu, *Carbon* **2019**, *144*, 370–381.
- [133] B. Qiu, M. Xing, J. Zhang, *Chem. Soc. Rev.* **2018**, *47*, 2165–2216.
- [134] S. Cai, R. Wang, W. Guo, H. Tang, *Langmuir* **2018**, *34*, 1992–1998.
- [135] Z. Wang, S. Peng, Y. Hu, L. Li, T. Yan, G. Yang, D. Ji, M. Srinivasan, Z. Pan, S. Ramakrishna, *J. Mater. Chem. A* **2017**, *5*, 4949–4961.
- [136] C. Tang, B. Wang, H.-F. Wang, Q. Zhang, *Adv. Mater.* **2017**, *29*, 1703185.
- [137] Y. Zheng, Y. Jiao, Y. Zhu, Q. Cai, A. Vasileff, L. H. Li, Y. Han, Y. Chen, S.-Z. Qiao, *J. Am. Chem. Soc.* **2017**, *139*, 3336–3339.
- [138] W. Zang, A. Sumboja, Y. Ma, H. Zhang, Y. Wu, S. Wu, H. Wu, Z. Liu, C. Guan, J. Wang, S. J. Pennycook, *ACS Catal.* **2018**, *8*, 8961–8969.
- [139] S. Li, C. Cheng, X. Zhao, J. Schmidt, A. Thomas, *Angew. Chem. Int. Ed.* **2018**, *57*, 1856–1862; *Angew. Chem.* **2018**, *130*, 1874–1880.
- [140] L. Yang, L. Shi, D. Wang, Y. Lv, D. Cao, *Nano Energy* **2018**, *50*, 691–698.
- [141] H. Xu, D. Cheng, D. Cao, X. C. Zeng, *Nat. Catal.* **2018**, *1*, 339–348.
- [142] P. Chen, T. Zhou, L. Xing, K. Xu, Y. Tong, H. Xie, L. Zhang, W. Yan, W. Chu, C. Wu, Y. Xie, *Angew. Chem. Int. Ed.* **2017**, *56*, 610–614; *Angew. Chem.* **2017**, *129*, 625–629.
- [143] L. Ma, S. Chen, Z. Pei, Y. Huang, G. Liang, F. Mo, Q. Yang, J. Su, Y. Gao, J. A. Zapien, C. Zhi, *ACS Nano* **2018**, *12*, 1949–1958.
- [144] P. Yin, T. Yao, Y. Wu, L. Zheng, Y. Lin, W. Liu, H. Ju, J. Zhu, X. Hong, Z. Deng, G. Zhou, S. Wei, Y. Li, *Angew. Chem. Int. Ed.* **2016**, *55*, 10800–10805; *Angew. Chem.* **2016**, *128*, 10958–10963.
- [145] C. Zhu, S. Fu, Q. Shi, D. Du, Y. Lin, *Angew. Chem. Int. Ed.* **2017**, *56*, 13944–13960; *Angew. Chem.* **2017**, *129*, 14132–14148.
- [146] Z. Zhang, J. Sun, F. Wang, L. Dai, *Angew. Chem. Int. Ed.* **2018**, *57*, 9038–9043; *Angew. Chem.* **2018**, *130*, 9176–9181.
- [147] X. Yan, D. Liu, H. Cao, F. Hou, J. Liang, S. X. Dou, *Small Methods* **2019**, DOI: 10.1002/smtd.201800501.
- [148] X. Han, X. Ling, Y. Wang, T. Ma, C. Zhong, W. Hu, Y. Deng, *Angew. Chem. Int. Ed.* **2019**, *58*, 5359–5364.
- [149] D. Deng, L. Yu, X. Chen, G. Wang, L. Jin, X. Pan, J. Deng, G. Sun, X. Bao, *Angew. Chem. Int. Ed.* **2013**, *52*, 371–375; *Angew. Chem.* **2013**, *125*, 389–393.
- [150] C.-Y. Su, H. Cheng, W. Li, Z.-Q. Liu, N. Li, Z. Hou, F.-Q. Bai, H.-X. Zhang, T.-Y. Ma, *Adv. Energy Mater.* **2017**, *7*, 1602420.
- [151] C. Tang, Q. Zhang, *J. Mater. Chem. A* **2016**, *4*, 4998–5001.
- [152] W.-J. Jiang, L. Gu, L. Li, Y. Zhang, X. Zhang, L.-J. Zhang, J.-Q. Wang, J.-S. Hu, Z. Wei, L.-J. Wan, *J. Am. Chem. Soc.* **2016**, *138*, 3570–3578.
- [153] H. Osgood, S. V. Devaguptapu, H. Xu, J. Cho, G. Wu, *Nano Today* **2016**, *11*, 601–625.
- [154] C. Wei, Z. Feng, G. G. Scherer, J. Barber, Y. Shao-Horn, Z. J. Xu, *Adv. Mater.* **2017**, *29*, 1606800.
- [155] Y. Zhu, W. Zhou, Z. Shao, *Small* **2017**, *13*, 1603793.
- [156] Y. Xue, S. Sun, Q. Wang, Z. Dong, Z. Liu, *J. Mater. Chem. A* **2018**, *6*, 10595–10626.
- [157] K. A. Stoerzinger, M. Risch, B. Han, Y. Shao-Horn, *ACS Catal.* **2015**, *5*, 6021–6031.
- [158] S. Zhao, T. Liu, D. Shi, Y. Zhang, W. Zeng, T. Li, B. Miao, *Appl. Surf. Sci.* **2015**, *351*, 862–868.
- [159] G. Cheng, S. Xie, B. Lan, X. Zheng, F. Ye, M. Sun, X. Lu, L. Yu, *J. Mater. Chem. A* **2016**, *4*, 16462–16468.
- [160] S. Ghosh, P. Kar, N. Bhandary, S. Basu, S. Sardar, T. Maiyalagan, D. Majumdar, S. K. Bhattacharya, A. Bhaumik, P. Lemmens, S. K. Pal, *Catal. Sci. Technol.* **2016**, *6*, 1417–1429.
- [161] K. Lei, L. Cong, X. Fu, F. Cheng, J. Chen, *Inorg. Chem. Front.* **2016**, *3*, 928–933.
- [162] F. Cheng, J. Shen, W. Ji, Z. Tao, J. Chen, *ACS Appl. Mater. Interfaces* **2009**, *1*, 460–466.
- [163] T.-H. Gu, D. A. Agyeman, S.-J. Shin, X. Jin, J. M. Lee, H. Kim, Y.-M. Kang, S.-J. Hwang, *Angew. Chem. Int. Ed.* **2018**, *57*, 15984–15989.
- [164] M. S. El-Deab, T. Ohsaka, *Angew. Chem. Int. Ed.* **2006**, *45*, 5963–5966; *Angew. Chem.* **2006**, *118*, 6109–6112.
- [165] T. Zhang, F. Cheng, J. Du, Y. Hu, J. Chen, *Adv. Energy Mater.* **2015**, *5*, 1400654.
- [166] T. Li, B. Xue, B. Wang, G. Guo, D. Han, Y. Yan, A. Dong, *J. Am. Chem. Soc.* **2017**, *139*, 12133–12136.
- [167] T. T. Truong, Y. Liu, Y. Ren, L. Trahey, Y. Sun, *ACS Nano* **2012**, *6*, 8067–8077.
- [168] X. Peng, K. Huo, J. Fu, B. Gao, L. Wang, L. Hu, X. Zhang, P. K. Chu, *ChemElectroChem* **2015**, *2*, 512–517.
- [169] G. Chen, F. Rosei, D. Ma, *Adv. Funct. Mater.* **2012**, *22*, 3914–3920.
- [170] T. Zhang, X. Ge, Z. Zhang, N. N. Tham, Z. Liu, A. Fisher, J. Y. Lee, *ChemCatChem* **2018**, *10*, 422–429.
- [171] Y. Zhao, J. Zhang, W. Wu, X. Guo, P. Xiong, H. Liu, G. Wang, *Nano Energy* **2018**, *54*, 129–137.
- [172] Y. Zhao, C. Chang, F. Teng, Y. Zhao, G. Chen, R. Shi, G. I. N. Waterhouse, W. Huang, T. Zhang, *Adv. Energy Mater.* **2017**, *7*, 1700005.
- [173] S. Chen, G. Liu, H. Yadegari, H. Wang, S. Z. Qiao, *J. Mater. Chem. A* **2015**, *3*, 2559–2563.
- [174] X. Zheng, L. Yu, B. Lan, G. Cheng, T. Lin, B. He, W. Ye, M. Sun, F. Ye, *J. Power Sources* **2017**, *362*, 332–341.
- [175] B. Lan, X. Zheng, G. Cheng, J. Han, W. Li, M. Sun, L. Yu, *Electrochim. Acta* **2018**, *283*, 459–466.
- [176] X. Ge, X. Song, Y. Ma, H. Zhou, G. Wang, H. Zhang, Y. Zhang, H. Zhao, P. K. Wong, *J. Mater. Chem. A* **2016**, *4*, 14814–14826.
- [177] L. Jin, L. Xu, C. Morein, C.-H. Chen, M. Lai, S. Dharmarathna, A. Dobley, S. L. Suib, *Adv. Funct. Mater.* **2010**, *20*, 3373–3382.
- [178] B. Liu, Y. Sun, L. Liu, S. Xu, X. Yan, *Adv. Funct. Mater.* **2018**, *28*, 1704973.
- [179] D. Chen, C. Chen, Z. M. Baiyee, Z. Shao, F. Ciucci, *Chem. Rev.* **2015**, *115*, 9869–9921.
- [180] Y. Liang, Y. Li, H. Wang, J. Zhou, J. Wang, T. Regier, H. Dai, *Nat. Mater.* **2011**, *10*, 780–786.
- [181] S. Mao, Z. Wen, T. Huang, Y. Hou, J. Chen, *Energy Environ. Sci.* **2014**, *7*, 609–616.
- [182] C. Guan, A. Sumboja, H. Wu, W. Ren, X. Liu, H. Zhang, Z. Liu, C. Cheng, S. J. Pennycook, J. Wang, *Adv. Mater.* **2017**, *29*, 1704117.
- [183] Y. Hao, Y. Xu, N. Han, J. Liu, X. Sun, *J. Mater. Chem. A* **2017**, *5*, 17804–17810.
- [184] Y. Li, C. Zhong, J. Liu, X. Zeng, S. Qu, X. Han, Y. Deng, W. Hu, J. Lu, *Adv. Mater.* **2018**, *30*, 1703657.
- [185] L. Zhu, D. Zheng, Z. Wang, X. Zheng, P. Fang, J. Zhu, M. Yu, Y. Tong, X. Lu, *Adv. Mater.* **2018**, *30*, 1805268.
- [186] J. Masa, W. Xia, I. Sinev, A. Zhao, Z. Sun, S. Grützke, P. Weide, M. Muhler, W. Schuhmann, *Angew. Chem. Int. Ed.* **2014**, *53*, 8508–8512; *Angew. Chem.* **2014**, *126*, 8648–8652.
- [187] X. Han, G. He, Y. He, J. Zhang, X. Zheng, L. Li, C. Zhong, W. Hu, Y. Deng, T.-Y. Ma, *Adv. Energy Mater.* **2018**, *8*, 1702222.
- [188] Z. Song, X. Han, Y. Deng, N. Zhao, W. Hu, C. Zhong, *ACS Appl. Mater. Interfaces* **2017**, *9*, 22694–22703.
- [189] Y. Yin, R. M. Rioux, C. K. Erdonmez, S. Hughes, G. A. Somorjai, A. P. Alivisatos, *Science* **2004**, *304*, 711–714.
- [190] B. Chen, X. He, F. Yin, H. Wang, D.-J. Liu, R. Shi, J. Chen, H. Yin, *Adv. Funct. Mater.* **2017**, *27*, 1700795.
- [191] G. Fu, X. Yan, Y. Chen, L. Xu, D. Sun, J.-M. Lee, Y. Tang, *Adv. Mater.* **2018**, *30*, 1704609.
- [192] X. Chen, L. Wei, Y. Wang, S. Zhai, Z. Chen, S. Tan, Z. Zhou, A. K. Ng, X. Liao, Y. Chen, *Energy Storage Mater.* **2018**, *11*, 134–143.
- [193] Y.-J. Li, L. Cui, P.-F. Da, K.-W. Qiu, W.-J. Qin, W.-B. Hu, X.-W. Du, K. Davey, T. Ling, S.-Z. Qiao, *Adv. Mater.* **2018**, *30*, 1804653.
- [194] A. Ajaz, J. Masa, C. Rösler, W. Xia, P. Weide, A. J. R. Botz, R. A. Fischer, W. Schuhmann, M. Muhler, *Angew. Chem. Int. Ed.* **2016**, *55*, 4087–4091; *Angew. Chem.* **2016**, *128*, 4155–4160.
- [195] X. Liu, M. Park, M. G. Kim, S. Gupta, X. Wang, G. Wu, J. Cho, *Nano Energy* **2016**, *20*, 315–325.

- [196] H. Cheng, M.-L. Li, C.-Y. Su, N. Li, Z.-Q. Liu, *Adv. Funct. Mater.* **2017**, *27*, 1701833.
- [197] Z.-Q. Liu, H. Cheng, N. Li, T. Y. Ma, Y.-Z. Su, *Adv. Mater.* **2016**, *28*, 3777–3784.
- [198] T. Ouyang, Y.-Q. Ye, C.-Y. Wu, K. Xiao, Z.-Q. Liu, *Angew. Chem. Int. Ed.* **2019**, *58*, 4923–4928.
- [199] A. Zhao, J. Masa, W. Xia, A. Maljusch, M.-G. Willinger, G. Clavel, K. Xie, R. Schlögl, W. Schuhmann, M. Muhler, *J. Am. Chem. Soc.* **2014**, *136*, 7551–7554.
- [200] S. Zeng, X. Tong, S. Zhou, B. Lv, J. Qiao, Y. Song, M. Chen, J. Di, Q. Li, *Small* **2018**, *14*, 1803409.
- [201] X.-R. Wang, J.-Y. Liu, Z.-W. Liu, W.-C. Wang, J. Luo, X.-P. Han, X.-W. Du, S.-Z. Qiao, J. Yang, *Adv. Mater.* **2018**, *30*, 1800005.
- [202] J. Suntivich, K. J. May, H. A. Gasteiger, J. B. Goodenough, Y. Shao-Horn, *Science* **2011**, *334*, 1383–1385.
- [203] E. Fabbri, M. Nachtegaal, X. Cheng, T. J. Schmidt, *Adv. Energy Mater.* **2015**, *5*, 1402033.
- [204] F. Calle-Vallejo, N. G. Inoglu, H.-Y. Su, J. I. Martínez, I. C. Man, M. T. M. Koper, J. R. Kitchin, J. Rossmeisl, *Chem. Sci.* **2013**, *4*, 1245–1249.
- [205] J. Suntivich, W. T. Hong, Y.-L. Lee, J. M. Rondinelli, W. Yang, J. B. Goodenough, B. Dabrowski, J. W. Freeland, Y. Shao-Horn, *J. Phys. Chem. C* **2014**, *118*, 1856–1863.
- [206] X. Xu, Y. Pan, W. Zhou, Y. Chen, Z. Zhang, Z. Shao, *Electrochim. Acta* **2016**, *219*, 553–559.
- [207] J.-I. Jung, H. Y. Jeong, J.-S. Lee, M. G. Kim, J. Cho, *Angew. Chem. Int. Ed.* **2014**, *53*, 4582–4586; *Angew. Chem.* **2014**, *126*, 4670–4674.
- [208] J. R. Petrie, V. R. Cooper, J. W. Freeland, T. L. Meyer, Z. Zhang, D. A. Lutterman, H. N. Lee, *J. Am. Chem. Soc.* **2016**, *138*, 2488–2491.
- [209] Y. Bu, O. Gwon, G. Nam, H. Jang, S. Kim, Q. Zhong, J. Cho, G. Kim, *ACS Nano* **2017**, *11*, 11594–11601.
- [210] W. T. Hong, M. Risch, K. A. Stoerzinger, A. Grimaud, J. Suntivich, Y. Shao-Horn, *Energy Environ. Sci.* **2015**, *8*, 1404–1427.
- [211] J.-I. Jung, S. Park, M.-G. Kim, J. Cho, *Adv. Energy Mater.* **2015**, *5*, 1501560.
- [212] J.-I. Jung, M. Risch, S. Park, M. G. Kim, G. Nam, H.-Y. Jeong, Y. Shao-Horn, J. Cho, *Energy Environ. Sci.* **2016**, *9*, 176–183.
- [213] I. Yamada, H. Fujii, A. Takamatsu, H. Ikeda, K. Wada, H. Tsukasaki, S. Kawaguchi, S. Mori, S. Yagi, *Adv. Mater.* **2017**, *29*, 1603004.
- [214] Y. Bu, H. Jang, O. Gwon, S. H. Kim, S. H. Joo, G. Nam, S. Kim, Y. Qin, Q. Zhong, S. K. Kwak, J. Cho, G. Kim, *J. Mater. Chem. A* **2019**, *7*, 2048–2054.
- [215] N.-I. Kim, R. A. Afzal, S. R. Choi, S. W. Lee, D. Ahn, S. Bhattacharjee, S.-C. Lee, J. H. Kim, J.-Y. Park, *J. Mater. Chem. A* **2017**, *5*, 13019–13031.
- [216] Y. Bu, G. Nam, S. Kim, K. Choi, Q. Zhong, J. Lee, Y. Qin, J. Cho, G. Kim, *Small* **2018**, *14*, 1802767.
- [217] J. T. Mefford, A. A. Kurilovich, J. Saunders, W. G. Hardin, A. M. Abakumov, R. P. Forslund, A. Bonnefont, S. Dai, K. P. Johnston, K. J. Stevenson, *Phys. Chem. Chem. Phys.* **2019**, *21*, 3327–3338.
- [218] Z. Chen, A. Yu, D. Higgins, H. Li, H. Wang, Z. Chen, *Nano Lett.* **2012**, *12*, 1946–1952.
- [219] Y. Yang, W. Yin, S. Wu, X. Yang, W. Xia, Y. Shen, Y. Huang, A. Cao, Q. Yuan, *ACS Nano* **2016**, *10*, 1240–1248.
- [220] X. Xu, W. Wang, W. Zhou, Z. Shao, *Small Methods* **2018**, *2*, 1800071.
- [221] J. E. Kim, J. Lim, G. Y. Lee, S. H. Choi, U. N. Maiti, W. J. Lee, H. J. Lee, S. O. Kim, *ACS Appl. Mater. Interfaces* **2016**, *8*, 1571–1577.
- [222] T. Zhan, Y. Zhang, X. Liu, S. Lu, W. Hou, *J. Power Sources* **2016**, *333*, 53–60.
- [223] Z. Li, M. Shao, Q. Yang, Y. Tang, M. Wei, D. G. Evans, X. Duan, *Nano Energy* **2017**, *37*, 98–107.
- [224] T. Zhan, X. Liu, S. Lu, W. Hou, *Appl. Catal. B: Environ.* **2017**, *205*, 551–558.
- [225] Y. Q. Jin, Z. Lin, R. Zhong, J. Huang, G. Liang, J. Li, Y. Jin, H. Meng, *J. Power Sources* **2018**, *402*, 388–393.
- [226] Q. Wang, L. Shang, R. Shi, X. Zhang, Y. Zhao, G. I. N. Waterhouse, L.-Z. Wu, C.-H. Tung, T. Zhang, *Adv. Energy Mater.* **2017**, *7*, 1700467.
- [227] Y. Lin, L. Yang, Y. Zhang, H. Jiang, Z. Xiao, C. Wu, G. Zhang, J. Jiang, L. Song, *Adv. Energy Mater.* **2018**, *8*, 1703623.
- [228] Y. Hao, Y. Xu, W. Liu, X. Sun, *Mater. Horiz.* **2018**, *5*, 108–115.
- [229] J. Lv, S. C. Abbas, Y. Huang, Q. Liu, M. Wu, Y. Wang, L. Dai, *Nano Energy* **2018**, *43*, 130–137.
- [230] S. Wang, G. Nam, P. Li, H. Jang, J. Wang, M. G. Kim, Z. Wu, X. Liu, J. Cho, *Nanoscale* **2018**, *10*, 15834–15841.
- [231] H. Li, Q. Li, P. Wen, T. B. Williams, S. Adhikari, C. Dun, C. Lu, D. Itanze, L. Jiang, D. L. Carroll, G. L. Donati, P. M. Lundin, Y. Qiu, S. M. Geyer, *Adv. Mater.* **2018**, *30*, 1705796.
- [232] F. Kong, X. Fan, A. Kong, Z. Zhou, X. Zhang, Y. Shan, *Adv. Funct. Mater.* **2018**, *28*, 1803973.
- [233] Y. Ding, Y. Niu, J. Yang, L. Ma, J. Liu, Y. Xiong, H. Xu, *Small* **2016**, *12*, 5414–5421.
- [234] H. Jiang, Y. Yao, Y. Zhu, Y. Liu, Y. Su, X. Yang, C. Li, *ACS Appl. Mater. Interfaces* **2015**, *7*, 21511–21520.
- [235] R. Nandan, K. K. Nanda, *J. Mater. Chem. A* **2017**, *5*, 16843–16853.
- [236] P. Ganeshan, M. Prabu, J. Sanetuntikul, S. Shanmugam, *ACS Catal.* **2015**, *5*, 3625–3637.
- [237] C. Hu, J. Liu, J. Wang, W. She, J. Xiao, J. Xi, Z. Bai, S. Wang, *ACS Appl. Mater. Interfaces* **2018**, *10*, 33124–33134.
- [238] B. Wang, C. Tang, H.-F. Wang, B.-Q. Li, X. Cui, Q. Zhang, *Small Methods* **2018**, *2*, 1800055.
- [239] D. Zhou, Y. Jia, H. Yang, W. Xu, K. Sun, J. Zhang, S. Wang, Y. Kuang, B. Liu, X. Sun, *J. Mater. Chem. A* **2018**, *6*, 21162–21166.
- [240] W. Niu, Z. Li, K. Marcus, L. Zhou, Y. Li, R. Ye, K. Liang, Y. Yang, *Adv. Energy Mater.* **2018**, *8*, 1701642.
- [241] Y. Li, Y. Zhou, H. Wen, J. Yang, C. Maouche, Q. Liu, Y. Wu, C. Cheng, J. Zhu, X. Cheng, *Dalton Trans.* **2018**, *47*, 14992–15001.
- [242] J. Wang, H. Liu, Y. Liu, W. Wang, Q. Sun, X. Wang, X. Zhao, H. Hu, M. Wu, *Carbon* **2019**, *144*, 259–268.
- [243] T. Liu, F. Yang, G. Cheng, W. Luo, *Small* **2018**, *14*, 1703748.
- [244] J. Fu, F. M. Hassan, C. Zhong, J. Lu, H. Liu, A. Yu, Z. Chen, *Adv. Mater.* **2017**, *29*, 1702526.
- [245] X. Han, X. Wu, C. Zhong, Y. Deng, N. Zhao, W. Hu, *Nano Energy* **2017**, *31*, 541–550.
- [246] X. Zheng, X. Han, H. Liu, J. Chen, D. Fu, J. Wang, C. Zhong, Y. Deng, W. Hu, *ACS Appl. Mater. Interfaces* **2018**, *10*, 13675–13684.
- [247] X. Wu, X. Han, X. Ma, W. Zhang, Y. Deng, C. Zhong, W. Hu, *ACS Appl. Mater. Interfaces* **2017**, *9*, 12574–12583.
- [248] C. Guan, A. Sumboja, W. Zang, Y. Qian, H. Zhang, X. Liu, Z. Liu, D. Zhao, S. J. Pennycook, J. Wang, *Energy Storage Mater.* **2019**, *16*, 243–250.
- [249] Q. Wang, L. Shang, R. Shi, X. Zhang, G. I. N. Waterhouse, L.-Z. Wu, C.-H. Tung, T. Zhang, *Nano Energy* **2017**, *40*, 382–389.
- [250] R. Akram, M. A. Ud Din, S. U. Dar, A. Arshad, W. Liu, Z. Wu, D. Wu, *Nanoscale* **2018**, *10*, 5658–5666.
- [251] M. Wu, Q. Wei, G. Zhang, J. Qiao, M. Wu, J. Zhang, Q. Gong, S. Sun, *Adv. Energy Mater.* **2018**, *8*, 1801836.
- [252] H.-F. Wang, C. Tang, B. Wang, B.-Q. Li, Q. Zhang, *Adv. Mater.* **2017**, *29*, 1702327.
- [253] X. Han, W. Zhang, X. Ma, C. Zhong, N. Zhao, W. Hu, Y. Deng, *Adv. Mater.* **2019**, DOI: 10.1002/adma.201808281.

Manuscript received: April 9, 2019

Version of record online: June 18, 2019